

**Doping of TiO₂ for sensitized solar cells**

Journal:	<i>Chemical Society Reviews</i>
Manuscript ID:	CS-SYN-04-2015-000352.R3
Article Type:	Review Article
Date Submitted by the Author:	17-Aug-2015
Complete List of Authors:	Roose, Bart; Adolphe Merkle Institute, Soft Matter Physics Pathak, Sandeep; University of Oxford, Physics Steiner, Ullrich; Adolphe Merkle Institute,

Doping of TiO₂ for sensitized solar cells

Bart Roose¹, Sandeep K. Pathak^{2*}, Ullrich Steiner^{1*}

¹ Adolphe Merkle Institute, Rue des Verdiers, CH-1700 Fribourg, Switzerland

² Clarendon Laboratory, Department of Physics, University of Oxford, Parks Road, Oxford, OX1 3PU, UK

Abstract

This review gives a detailed summary and evaluation of the use of TiO₂ doping to improve the performance of dye sensitized solar cells. Doping has a major effect on the band structure and trap states of TiO₂, which in turn affect important properties such as the conduction band energy, charge transport, recombination and collection. The defect states of TiO₂ are highly dependent on the synthesis method and thus the effect of doping may vary for different synthesis techniques, making it difficult to compare the suitability of different dopants. High-throughput methods may be employed to achieve a rough prediction on the suitability of dopants for a specific synthesis method. It was however found that nearly every employed dopant can be used to increase device performance, indicating that the improvement is not so much caused by the dopant itself, as by the defects it eliminates from TiO₂. Furthermore, with the field shifting from dye sensitized solar cells to perovskite solar cells, the role doping can play to further advance this emerging field is also discussed.

1 Introduction

To keep up with future demand for energy it will be necessary to deploy clean, renewable sources on a massive scale [1, 2]. One promising option is the large scale application of photovoltaic devices, which generate electricity directly from sunlight [3]. This has so far been limited because of the high cost associated with the production of these devices [2, 4, 5]. In the last decades many new photovoltaic technologies have been developed, promising low cost, high-throughput processing which will pave the way to affordable renewable energy [1, 2, 5, 6]. One of the leading candidates is the dye sensitized solar cell (DSSC) [7–9], in particular the perovskite-based solar cell,

which is closely related to devices employing organic dyes [10–13]. Perovskite solar cells currently have a NREL certified record efficiency of more than 20% [6], with a marked upward trend. This is in the efficiency range needed for commercially viable applications [14].

Major challenges remain however in scaling up the fabrication from the laboratory to industrial production [15, 16], addressing toxicity issues [17–19], reducing hysteresis [17, 20, 21] and in particular regarding the achievement of sufficiently high device lifetimes [13, 20]. The control over the device properties and how they can be reliably achieved requires a better understanding of the underlying chemistry and physics. Ever since the first report of DSSCs, best performing devices have relied on titanium dioxide (TiO₂) as nanostructured electron transporting layer and/or hole blocking layer [22, 23]. Extensive research has been done to control the morphology of the TiO₂ with the aim of maximizing the dye-TiO₂ interface area and light absorption [24–26]. With the recent optimization of dyes, hole-conductors and device architectures the focus has shifted to controlling the electronic properties of TiO₂. Mesoporous TiO₂ is full of lattice defects that arise during synthesis, resulting in a multitude of electronic sub-band gap states that are able to trap charges [8, 9].

Here we discuss how these defects affect the electronic properties of TiO₂ and how they can be influenced by doping, that is by deliberately introducing impurities into TiO₂. In photocatalytic materials this is a well known method to increase the spectral response and promote the separation of charges [27–29]. From these studies it is evident that not only the type of dopant is important but also where the dopant is situated in the TiO₂-lattice. Another way to control recombination processes is to cover TiO₂ with a thin layer of insulating oxide [30], this is however outside the scope of this review.

First the general working principle of DSSCs and the properties of TiO₂ are elucidated. This is

followed by a detailed overview of results that have been achieved so far using different dopants and doping techniques. Then, we assess what can be learned from these doping studies and how doping can be implemented to achieve better performance in perovskite solar cells. Finally, the tools that can be used to investigate the (electronic) properties of TiO_2 and the effects of doping are summarized.

2 Working principle of DSSCs

The first working example of a DSSC was reported by O'Regan and Grätzel in 1991 [7]. The same device architecture is still employed today and consists of the following components (top to bottom of Figure 1a):

- Transparent conducting oxide (TCO) coated glass. Typical TCOs are tin-doped indium oxide (ITO) and fluorine-doped tin oxide (FTO).
- Hole blocking layer (HBL), a continuous layer of a metal oxide that prevents holes from reaching the TCO, shorting the device.
- Electron transporting material consisting of a mesoporous metal oxide, which is usually TiO_2 . Several other metal oxides such as SnO_2 [31], ZnO [32, 33] and SrTiO_3 [34] have also been explored, but none of them perform as well as TiO_2 .
- Dye adsorbed to the mesoporous metal oxide, which is responsible for absorbing light. Because the adsorbed dye usually consists of only a monolayer, a several micrometer thick mesoporous layer is needed to provide sufficient surface area to absorb most of the light.
- Liquid electrolyte or solid-state hole transporting material (HTM), which is infiltrated into the mesoporous layer. Liquid electrolytes often contain the iodide/triiodide redox couple. A problem using liquid electrolytes is the possible leakage of the corrosive fluid. Solid-state HTMs do not suffer from this problem but feature lower device efficiencies. A typical HTM is 2,2',7,7'-tetrakis(N,N'-dimethoxyphenylamine)-9,9'-spirobifluorene (spiro-OMeTAD).
- Back contact consisting of a metal electrode.

When the device is illuminated the dye is excited, promoting electrons from the highest occupied molecular orbital (HOMO) to the lowest unoccupied molecular orbital (LUMO). This excited state injects electrons into the conduction band (CB) of TiO_2 , which diffuse through the mesoporous scaffold to the TCO. The holes are transferred from the HOMO of the dye to the HTM and from there to the back electrode (Figure 1b).

The three important quantities governing the efficiency of a solar cell are the short circuit current J_{SC} , the open circuit voltage V_{OC} and the fill factor FF . J_{SC} is the current through the device in the absence of a net voltage, that is for a short-circuited device. It is highly dependent on light absorption and charge collection efficiency. V_{OC} is the voltage across the device in the absence of a net current. It depends on the energy difference between the Fermi levels (E_{F}) of the TiO_2 CB and HTM valence band (VB) or HOMO, and on recombination processes. The fill factor quantifies the power that can be delivered by the device. It is defined by dividing the maximum power output by $J_{\text{SC}} \times V_{\text{OC}}$. Its magnitude depends on series and shunt resistances in the device. A low series resistance and high shunt resistance minimize internal losses, thereby maximizing the power output of the device.

To obtain maximum efficiencies, it is important to match the CB of TiO_2 to the LUMO of the dye so that the potential difference is sufficiently large for electron injection, while keeping the difference between the CB of TiO_2 and the VB of the HTM as large as possible to maximize V_{OC} .

3 TiO_2

The large band gap, suitable band edge levels for charge injection and extraction, the long lifetime of excited electrons, exceptional resistance to photo corrosion, non-toxicity and low cost have made TiO_2 a popular material for solar energy applications [27–29].

TiO_2 occurs naturally in three crystalline forms; anatase (tetragonal), rutile (tetragonal) and brookite (orthorhombic). For DSSCs, anatase is the most commonly used phase due to its superior charge transport. The tetragonal anatase crystal structure is made up of a chain of distorted TiO_6 octahedrons, which results in a unit cell containing four Ti atoms (at positions $[0,0,0]$, $[\frac{1}{2}, \frac{1}{2}, \frac{1}{2}]$, $[0, \frac{1}{2}, \frac{1}{4}]$ and $[\frac{1}{2}, 0, \frac{3}{4}]$) and eight O atoms [26, 35, 36] (Figure 2).

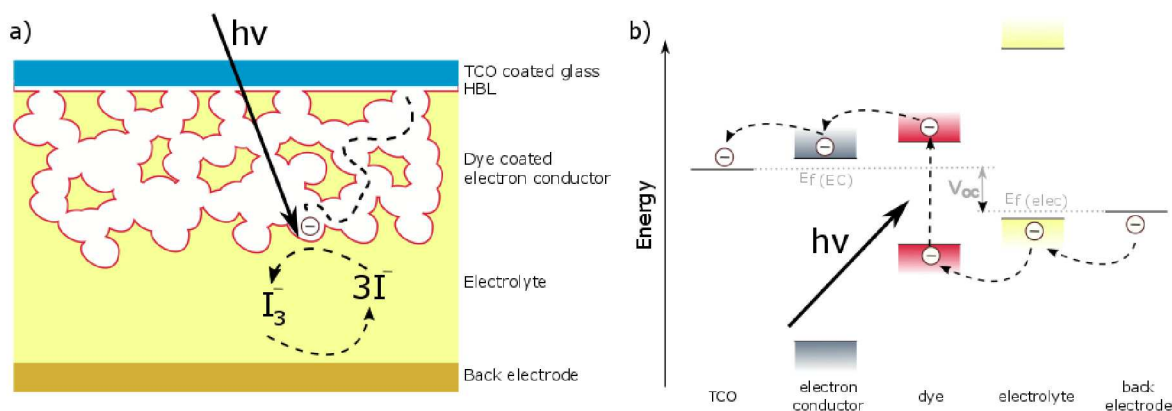


Figure 1: a) Schematic of DSSC device architecture, consisting of (top to bottom): transparent conducting oxide (TCO) coated glass; continuous metal oxide hole blocking layer (HBL); electron conductor coated with dye; liquid electrolyte or solid-state hole transporting material (HTM); metal back electrode. Upon the absorption of light, electrons and holes are created, which are transported through the respective transporting materials to the electrodes. b) Charge transport in a DSSC: upon absorption of light by the dye, an electron is excited from the HOMO to the LUMO, injected into the CB of the electron conductor (TiO_2) and transported to the TCO electrode. The dye is regenerated by oxidation of iodide to tri-iodide. In the case of a solid-state HTM, the hole is transported through the HTM to the electrode

TiO_2 prepared by sol-gel processes is amorphous and annealing at elevated temperatures is required to achieve the desired crystal structure. The crystallization temperature is limited by the anatase-rutile transition. Since rutile is the thermodynamically most stable polymorph of TiO_2 at all temperatures, the anatase to rutile transition temperature depends sensitively on preparation conditions. Because of their different band structures, mixed phases of anatase and rutile generally cause the trapping of charge carriers and promote recombination processes. They are mostly undesirable in DSSC electrodes, although there are some studies suggesting a small amount of rutile nanoparticles can enhance device performance [37–39]. DSSCs employing rutile TiO_2 generally suffer from a lower CB compared to anatase, leading to a lower V_{OC} . In addition, reduced dye adsorption and charge transport lower the obtainable J_{SC} [40–42]. Because of these complications, rutile is not frequently used in DSSCs, although there are some examples which are discussed in Section 4 [43, 44].

The band gap of n-type semiconducting single-crystal anatase TiO_2 is approximately 3.2 eV and the resistivity is $\sim 10^{15} \Omega\text{cm}$ [45]. The lower edge of the CB is made up of vacant Ti^{4+} 3d bands and the upper edge of the VB is made up of filled O^{2-} 2p bands [46]. Bulk oxygen vacancies, titanium

interstitials and reduced crystal surfaces generate shallow electron traps that can enhance the conductivity of TiO_2 . Of particular interest here is the occurrence of Ti^{3+} species, which form a band roughly 0.5 eV below the TiO_2 CB. These defects act as n-type dopants, increasing the number of free electrons in the TiO_2 and hence the conductivity and current. At the same time defects can act as charge trap and are therefore recombination centers, having a negative effect on device performance [45, 47].

The number of defects can be influenced by moderately heating the device or by placing it in an inert atmosphere [48]. Furthermore, it was discovered that the number of traps can be reversibly changed by oxygen exposure or deprivation, indicating oxygen can adsorb onto TiO_2 defects and by doing so passivate trap states. A further remarkable observation is that UV irradiation causes the desorption of oxygen from these defects. Under exposure to air, oxygen release is counterbalanced by oxygen adsorption from the atmosphere. DSSCs are however typically protected from moisture and dye degradation by air-free encapsulation. The lack of oxygen inside the encapsulated device upsets the desorption-adsorption balance, leading to an increase in trap states and deterioration of device properties. This again is reversible upon breaking the seal and exposure to

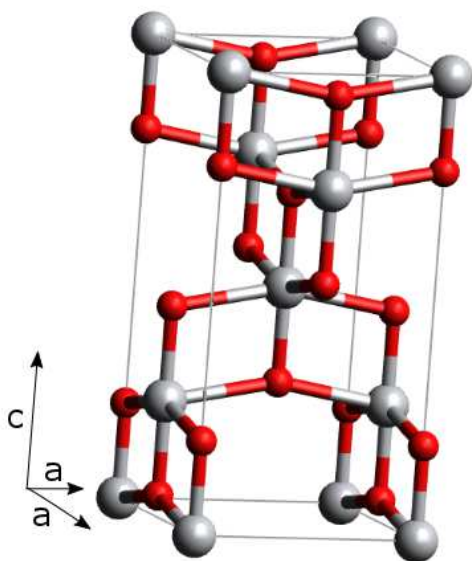


Figure 2: The anatase unit cell; titanium atoms are grey, oxygen atoms are red. Oxygen atoms form a distorted octahedron with a titanium atom at the center, which is clearly illustrated for the central titanium atom.

oxygen [49–51].

Because of its many defects and the resulting sub-band gap states in TiO_2 , electron transport is complex and hard to investigate. In devices, this is particularly difficult because parameters relating to one device property can not be studied individually without significantly changing other material properties. There is however strong theoretical and experimental evidence indicating that charge transport in TiO_2 proceeds by detrapping from sub-band gap states. These states lie deep in the tail of the density of states (DOS), from which electrons can be detrapped into the CB, according to the multiple-trapping model for charge transport [8]. The occupation of sub-band gap states at energy E_A can be found through the Fermi-Dirac distribution function

$$F(E_A - E_{Fn}) = \frac{1}{1 + e^{(E_A - E_{Fn})/k_b T}} \quad (1)$$

and the density of carriers at the energy E_A is $n_A = N_A F_A$, where N_A is the total number of available trap sites at this energy. From this, the density of electrons in the CB (n_{CB}) can be derived as a function of the position of the quasi-Fermi level for electrons (E_{Fn}),

$$n_{CB} = N_{CB} e^{(E_{Fn} - E_{CB})/k_b T} \quad (2)$$

Considering electron transport takes place only in

the CB, the conductivity of the film is given by

$$\sigma = n_{CB} e \mu, \quad (3)$$

where μ is the electron mobility. Generally, a higher TiO_2 conductivity means a higher current output from the device. From the equations above it is apparent that the conductivity of the film is determined by the probability of the electrons being in the CB, which increases as the quasi-Fermi level approaches the CB. This means that any modification that eliminates deep trap states will increase the conductivity of the film [8].

To be able to effectively modify the trap states it is important to know where the traps are located. Different studies have suggested traps are located either in the bulk [52], at inter-particle grain boundaries [53] or at the surface of the particles [54, 55]. Bulk defects do not seem to play a major role [56] and it should be noted that charge recombination is an interfacial process [57]. But because of the difficulty to experimentally distinguish between boundary or surface defects it is still unclear where exactly the traps are located [8] and it can not be excluded that both traps at the grain boundaries and at the TiO_2 surface play an equally important role. Furthermore the synthesis method heavily affects defect locations and type. This makes it difficult to effectively modify the TiO_2 structure. It is understood that weakly reducing synthesis conditions and low annealing temperatures favor the formation of oxygen vacancies, whereas more reducing synthesis conditions and high annealing temperatures favor titanium interstitials as main defects [26, 45].

This combination of factors leads to the complex situation where shallow traps are essential for charge transport and can actually improve conductivity, but at the same time, deep traps lower the quasi-Fermi level and decrease conductivity. The voltage of the device, which is defined as the energy difference between the quasi-Fermi levels of TiO_2 and the HTM, is also affected by the trap states, with less deep traps resulting in a higher open circuit voltage. Furthermore, traps can act as recombination sites for electrons and holes [26], which leads to a decrease in both current and voltage.

At the interface between TiO_2 and the HTM, band bending occurs due to the formation of a space charge region, implying that the CB in the bulk and at the surface do not have the same energy. The space charge region provides an electric field that separates electrons and holes. An exter-

nal voltage can cancel out band bending and eliminate the space charge region. This specific voltage is called the flat-band potential V_{FB} [58]. Because trap states are predominantly located on the TiO_2 surface they have a large influence on V_{FB} and thereby on the separation efficiency of electrons and holes. When V_{FB} is negatively shifted (indicating an upward shift of the conduction band and the Fermi level), the injection of electrons from the dye into TiO_2 will become less efficient and a loss in current occurs. The reverse is also true and some defects make injection more efficient by positively shifting V_{FB} , causing a downward shift of the conduction band and Fermi level. With so many interconnected processes it is clear that devising a method to improve the electronic properties of TiO_2 is not trivial.

TiO_2 nanostructures for DSSCs can be synthesized in several ways, the most common methods discussed in this review are:

- *Sol-Gel Synthesis.* The sol-gel method is a versatile process that can be employed to make nanoparticles of ceramic materials. A colloidal suspension (sol) is made by hydrolyzing and polymerizing metal oxide precursors. The precursor typically is an inorganic metal salt or a metal organic compound. Frequently used precursors for TiO_2 are titanium tetrachloride ($TiCl_4$) and titanium isopropoxide (TTIP). When the polymerization is complete and the solvent has evaporated, the sol forms a gel. Heat treatment will transform the gel into the desired TiO_2 nanoparticle [26].
 - *Hydrothermal Synthesis.* For the hydrothermal method a titanium precursor (TTIP) is mixed with water and a peptizer (HNO_3) after which the mixture is treated in an autoclave at elevated temperatures and pressures. After autoclaving the mixture is calcined to obtain TiO_2 nanoparticles [26].
 - *Solvothermal Synthesis.* The solvothermal method is similar to the hydrothermal method, with the exception that the used solvent is non-aqueous. By choosing high boiling point solvents it is possible to achieve much higher temperatures, increasing the control over the particle formation [26].
 - *Flame Spray Pyrolysis.* For flame spray pyrolysis (FSP) titanium precursor is dissolved in a solvent to generate a source solution. This solution is vaporized using a spray nozzle onto a substrate which is kept at elevated temperatures (300-500 °C). During spraying the solvent evaporates due to the elevated temperature and nanoparticles are formed [59].
 - *Anodization.* TiO_2 nanotubes can be grown directly from titanium metal by applying a potential to a metal foil in a fluoride containing electrolyte solution. The tube length and diameter can be controlled through the anodization time and potential, electrolyte composition and pH. The amorphous nanotubes are then annealed at elevated temperatures to achieve crystalline TiO_2 nanotubes [25, 26, 60].
 - *Micelle Method.* With the help of surfactants, micelles of TiO_2 precursor are formed in solution. Upon heat treatment these are converted to TiO_2 nanoparticles [26].
 - *Direct Oxidation.* Titanium can be treated with oxidising agents to yield TiO_2 nanostructures [61], similar to anodization.
 - *Sonochemical Synthesis.* Applying ultrasound to a solution can cause intense local heating, high pressures and enormous heating and cooling rates. This can be used to synthesize TiO_2 nanoparticles with high aspect ratios [26, 62].
 - *Microwave Synthesis.* Electromagnetic radiation can be used to heat up dielectrics to form nanostructures. A major advantage is the fast processing times due to the rapid heat transfer [63].
 - *Electrospinning.* An electrical charge is used to draw fibres from a solution, resulting in TiO_2 nanostructures with high aspect ratios [64].
- Compact TiO_2 films for electron blocking layers are synthesized through the following methods:
- *Spin Coating.* A solution of TiO_2 precursor is spin coated on a substrate to form a thin layer of compact TiO_2 [65].
 - *Spray Pyrolysis.* This method is similar to that described for the synthesis of TiO_2 nanoparticles, with the exception that the particles form a dense layer on the substrate [66].

- *Atomic Layer Deposition.* A substrate is alternately exposed to a TiO_2 precursor and H_2O , resulting in the deposition of atomically thick layers. The thickness of the layer can accurately be controlled through the number of cycles [67].
- *Thermal Oxidation.* A thin layer of titanium is deposited by sputtering or evaporation and subsequently heated to high temperatures in the presence of oxygen to oxidize the film which forms a compact TiO_2 layer [68].
- *Electrochemical Deposition.* A compact layer of TiO_2 can be deposited from a TiO_2 precursor solution by electrochemical deposition. The layer is subsequently crystallized by heating [69].
- *Pulsed Laser Deposition.* For pulsed laser deposition a TiO_2 precursor is pressed to form a disk which is used as a laser target. The laser vaporizes the target and the vapor condenses on the substrate forming a thin layer [70, 71].

4 Doping

An effective way of modifying the electronic properties of TiO_2 is doping [72], the deliberate insertion of impurities into the TiO_2 -lattice. In silicon solar cells, doping is a frequently used method to improve conductivity. Here the effect can mainly be ascribed to the increase in free charges and thus conductivity, by the donation of electrons for dopants with a valency higher than that of the native material (n-type doping), or holes for dopants with a lower valency (p-type doping). In the case of TiO_2 the mechanism is much more complicated due to the defect ridden nature of TiO_2 and doping mainly affects the trap states and electronic structure of TiO_2 , which is illustrated by the improvements that are made by doping with elements of equal valency as the host TiO_2 ions [73]. Doping can be achieved by either replacing the Ti^{4+} cation or the O^{2-} anion. Cationic dopants are typically metals, whereas anionic dopants are non-metals. Since the lower edge of the CB is made up of Ti^{4+} 3d bands, replacing Ti^{4+} by a different cation is thus expected to heavily affect the CB structure. The upper edge of the VB consists of O^{2-} 2p bands and replacing O^{2-} by a different anion affects the VB energy.

The atomic radius of the dopant should not differ much from the ion it replaces to prevent lattice

distortion, introducing new defects that may hamper device performance.

Because dye molecules anchor to Ti atoms [74], the replacement of Ti with another cation also affects dye adsorption due to different binding strengths between the dye and the dopant, or because the dopant induces oxygen vacancies [75]. Dopants often inhibit the growth rate of the TiO_2 nanoparticles, resulting in smaller particles [76]. This is in many cases beneficial since assemblies made from smaller particles have a larger surface area per volume of mesoporous TiO_2 compared to large particle assemblies. The increased surface area accommodates more dye, leading to higher light absorption and current densities. The main advantage of high light absorption is that thinner films can be used in photovoltaic devices, resulting in a reduction of recombination, which benefits both J_{SC} and V_{OC} .

Morphology is a further factor that influences the properties of TiO_2 . One-dimensional structures such as nanotubes have superior charge transport over nanoparticle assemblies, but have less surface area and thus adsorb less dye [77]. This implies that one-dimensional structures will benefit more from dopants that increase dye adsorption, whereas nanoparticle assemblies will benefit more from doping that leads to increased charge transport. The dopant source can also influence the effectiveness of doping and it has been shown that organic sources lead to better performances than inorganic salts [78]. Furthermore, doping influences the anatase to rutile phase transition [79]. The above factors complicate the study of the effect of doping on the electronic properties of TiO_2 as it is hard to distinguish and quantify whether an improvement is caused by increased absorption or electronic effects.

The dopant can be introduced into the TiO_2 -lattice in a number of ways:

- The most common method is simply mixing a dopant precursor with the TiO_2 precursor solution. This method can be employed in the sol-gel, hydrothermal, solvothermal, spray pyrolysis, atomic layer deposition, electrochemical deposition, sonochemical, microwave and electrospinning methods [35].
- For pulsed laser deposition a dopant precursor is mixed with the titanium precursor and pressed to form a disk that can be used as a target for the laser [70, 71].
- By immersing the final TiO_2 -structure into

an electrolyte solution containing the dopant and applying a voltage to electrochemically dope the TiO_2 [80].

- For anodization and thermal oxidation, a Ti-dopant alloy can be used [25, 60].

The dopants can be grouped into separate categories that share common electronic configurations. These are (earth)alkali metals (Section 4.1), metalloids (Section 4.2), non-metals (Section 4.3), transition metals (Section 4.4), post-transition metals (Section 4.5) and lanthanides (Section 4.6).

In some cases co-doping with two or more dopants is applied to further increase device performance. Each dopant can separately enhance device properties [81]. One dopant can reinforce the effect of the other dopant [82], or one dopant may counteract some of the detrimental effects caused by the other dopant [83].

4.1 (Earth)alkali metals

The outer electron shell of the metals in this group consists of s electrons which can be easily donated [84], making these metals interesting cationic dopants for TiO_2 . The earth-alkali metals that have been used for TiO_2 doping are lithium [85, 86], magnesium [87–90] and calcium [91–93].

4.1.1 Lithium

Using electrochemical impedance spectroscopy (EIS) and Hall effect measurements, it was found that Li^+ -doping increases conductivity and charge densities in TiO_2 , resulting in an increased J_{SC} . Fourier transform infrared (FTIR) spectroscopy indicated Li^+ is incorporated interstitially. It is suggested the observed V_{OC} increase arises from a negative V_{FB} shift, increasing E_{F} and CB (Figure 3b) [85].

To investigate the effect of particle size on doping, three different sized particles (22, 14 and 6 nm) were synthesized. In large particles bulk doping was dominant, while small particles exhibited mainly surface doping, as confirmed by x-ray diffraction (XRD). For the larger two particle sizes Li^+ -doping decreased device efficiencies, while efficiencies increased for the smallest particle size. The loss in efficiency is ascribed to the formation of Ti^{3+} species in the bulk that permanently trap electrons and decrease photocurrents. The enhanced efficiency for the smallest particle size is attributed to the Li^+ ions at the

surface acting as temporary electron traps, which increases the electron lifetime and reduces recombination (EIS). V_{OC} increases for all sizes caused by a band edge shift instigated by surface Li^+ adsorption [86]. The fact that doped small particles yield less efficient devices compared to undoped large particles (generally a decrease in particle size results in an increase in dye adsorption and efficiency) is an indication that several factors are playing a role, not only Li^+ -doping. The large particles were obtained from commercial sources and contained substantial amounts of rutile, while the small particles were synthesized using a hydrothermal method and were pure anatase. This results in different TiO_2 particles that will not react similarly to doping.

In addition, Li^+ ions from the electrolyte can adsorb onto and intercalate into TiO_2 , resulting in a positive shift of the CB (Figure 3c) and reduced recombination [94, 95].

4.1.2 Magnesium

A high V_{OC} of up to 1.2 V was reached by doping TiO_2 with Mg^{2+} [87, 88]. A more detailed study showed Mg^{2+} is introduced substitutionally and decreases particle size. UV/Vis absorption spectroscopy showed a widening of the band gap indicating an upward shift of CB. This leads to an increase in V_{OC} , but because of decreased electron injection and lifetime J_{SC} is reduced [89].

Zn/Mg co-doped devices showed no effect on the optical band gap or V_{OC} . There is a positive shift in V_{FB} , indicating a lowering in E_{F} and CB (Figure 3c), and an increase in recombination sites, which might be compensated by faster electron transport. The faster transport, in combination with enhanced electron injection due to the shift of CB resulted in a marked increase in J_{SC} [90].

4.1.3 Calcium

Doping TiO_2 with Ca^{2+} was shown to drastically improve J_{SC} , but this was accompanied by a loss in V_{OC} . Mott-Schottky plots showed a positive shift of V_{FB} (Figure 3c) and an increased carrier density, which is associated with increased electron injection and higher J_{SC} , but at a loss in V_{OC} . Intensity-modulated photo current spectroscopy (IMPS) showed an increased electron mobility, which further increased J_{SC} [91]. Other studies showed similar increases in J_{SC} . By using a low doping concentration V_{OC} was unaffected [92] or even improved by reducing the recombination

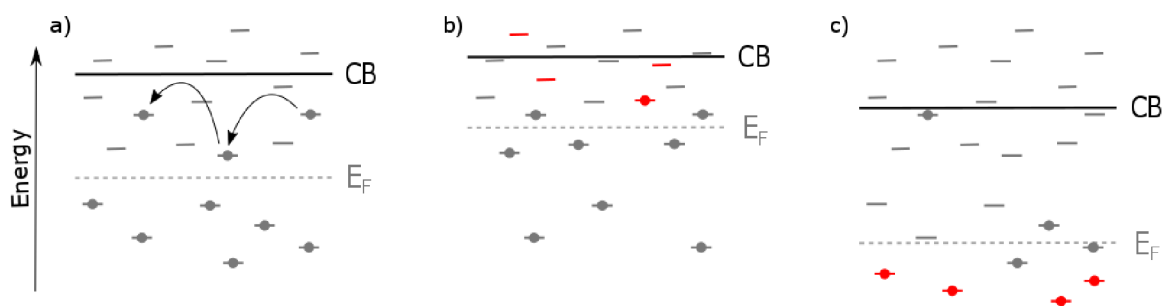


Figure 3: The effect of TiO_2 doping on the CB and E_F . The doping induced states are shown in red. a) In pristine TiO_2 , electrons are transported by ‘hopping’ from shallow trap to shallow trap until they reach the electrode. The shallow trap density will thus influence electron transport rate and J_{SC} . Deep traps can permanently trap electrons and act as recombination sites, affecting V_{OC} . Another important factor determining V_{OC} is E_F , as V_{OC} is defined as the difference between E_F of TiO_2 and the HTM. b) Doping can decrease the deep trap density, resulting in an upward shift of E_F and thus an increase of V_{OC} . The elimination of deep traps retards recombination and boosts the V_{OC} even further. Because the CB is shifted towards the LUMO of the absorber, the driving force for electron injection is lowered, in combination with a decreased trap density and the related electron transport, lowering J_{SC} . c) When doping contributes to the formation of deep traps, the conduction band and E_F are shifted downwards. In combination with enhanced recombination through the deep trap states V_{OC} decreases. Because of the larger offset between the CB and the absorber LUMO, electron injection is improved and the higher trap density causes an increase in electron transport, resulting in an enhanced J_{SC} . Ideally, the dopant eliminates deep traps while introducing new states close to CB, enhancing both V_{OC} and J_{SC} through decreased recombination and increased electron transport.

rate [93].

4.2 Metalloids

The elements that belong to the metalloid group have properties that lie between metals and non-metals, offering the possibility to combine the positive doping effects of metals and non-metals [96]. Metalloids regularly used for doping are boron [97–100], silicon [101], germanium [102] and antimony [83, 103].

4.2.1 Boron

Scanning electron microscopy (SEM) and XRD showed an increase in TiO_2 crystallinity upon B^{3+} -doping, which is beneficial for electron transport. X-ray photoelectron spectroscopy (XPS) indicated that B^{3+} is incorporated both substitutionally and interstitially. Interstitial doping has been reported to be accompanied by a blue shift of the UV/Vis absorption spectrum [104] and an increase in oxygen vacancies [105], which was confirmed by UV/Vis and electron paramagnetic resonance (EPR) spectroscopy. EIS showed an increase in electron recombination, which compen-

sates the negatively shifted V_{FB} (Figure 3b) and leaves V_{OC} unchanged. J_{SC} is increased due to the increased electron transport [97–99]. Another study also reported improved crystallinity and interstitial doping for TiO_2 nanotubes. However, a red shifted absorption spectrum was also reported in this study and although recombination was retarded, a lower V_{OC} was observed. A shift in V_{FB} allowed for better charge injection, which in combination with improved crystallinity led to increased J_{SC} [100].

4.2.2 Silicon

XRD showed increased crystallinity for Si^{4+} doped TiO_2 , which should have a positive effect on electron transport and recombination [101].

4.2.3 Germanium

XRD and gas absorption surface area analysis (BET) indicate a decrease in particle size and an increase in surface area upon Ge^{4+} doping of TiO_2 , resulting in higher values of J_{SC} . V_{FB} shows a negative shift (Figure 3b), which results in an increase in V_{OC} [102]. Electron injection is probably

reduced by this shift in V_{FB} , limiting J_{SC} .

4.2.4 Antimony

The introduction of Sb^{3+} into TiO_2 did not affect the particle size, as measured by XRD. UV/Vis absorption spectroscopy showed a small decrease in band gap and V_{FB} was shifted positively (Figure 3c), resulting in a reduction of V_{OC} , which is in part compensated by reduced recombination. Despite a decrease in electron density and lifetime, the charge collection efficiency increased due to faster electron transport. Together with enhanced electron injection due to a lower V_{FB} , the faster electron transport resulted in increased J_{SC} [103]. This trend was confirmed by a second study, which also showed that the drop in V_{OC} can be compensated by co-doping with Cr^{3+} , due to electron transfer from Sb to Cr, preventing the formation of oxygen vacancies and Ti^{3+} species [83].

4.3 Non-metals

Characteristic properties of non-metals are high ionization energies and high electro negativity. Because of these properties non-metals usually gain electrons when reacting with other compounds, forming covalent bonds. Among the non-metals are the only anionic dopants, which have a strong influence on the VB. Non-metal dopants are carbon [99, 106, 107], nitrogen [82, 98, 99, 107–143], fluorine [99, 141, 144–147], sulphur [82, 118, 120, 128] and iodine [148].

4.3.1 Carbon

Carbon was mainly incorporated interstitially, as measured by XPS, and resulted in a red shift in the UV/Vis spectrum. This is indicative of narrowing of the band gap, resulting in an increase in J_{SC} [106]. IMPS and intensity-modulated photovoltage spectroscopy (IMVS) showed increased transport rates and electron lifetimes, further contributing to increased values of J_{SC} and V_{OC} [99, 107].

4.3.2 Nitrogen

Nitrogen doping usually causes a red shift of the absorption band edge [82, 108–119] instigated by a positive shift of V_{FB} (Figure 3c), which improves electron injection [120]. Increased dye adsorption resulted in higher J_{SC} values. XPS studies showed that N^{3-} was introduced both substitutionally (replacing oxygen) and interstitially [121],

which was confirmed by EPR [122]. The introduction of N^{3-} distorts the lattice and was reported to lower charge transport [123, 124]. Most studies have however report increased charge transport rates [107, 125–132] and/or longer lifetimes [99, 133–143], leading to an increase in J_{SC} and V_{OC} .

Negative shifts in V_{FB} (Figure 3b) have been reported for Boron co-doped TiO_2 , in combination with retarded recombination leading to a marked increase in V_{OC} [98, 99].

4.3.3 Fluorine

Fluorine-doping reduced the interfacial resistance between the TiO_2 blocking layer and FTO, significantly improving J_{SC} [144]. In mesoporous TiO_2 a decreased defect density was found, while crystallinity increased and the formation of brookite was inhibited. Improved crystallinity led to an increase in J_{SC} [145]. I - V curves in the dark showed a decrease in parasitic resistances, leading to a marked increase in FF. EIS showed prolonged electron lifetimes, indicating that recombination was retarded, resulting in an increase in V_{OC} [99, 146, 147]. Co-doping with Nb^{5+} , Sn^{4+} , Sb^{3+} or Ta^{5+} resulted in a further increase in electron transport and decrease in recombination [147]. A positive shift of V_{FB} (Figure 3c) was reported to enhance electron injection while recombination was reduced [141].

4.3.4 Sulphur

Sulphur is often used as a co-dopant for N-doping to further decrease the band gap energy and increase light absorption [82, 118, 120, 128].

4.3.5 Iodine

Doping of TiO_2 with I^{5+} can enhance light absorption and decrease recombination [149, 150]. Dye adsorption studies showed that the amount of adsorbed dye is not significantly changed. UV/Vis spectroscopy showed a distinct absorption red shift upon doping, indicating a decrease in the band gap energy. This leads to more efficient electron injection and higher J_{SC} . EIS evidenced a decreased recombination rate, resulting in a higher V_{OC} [148]. DFT calculations predict that I^{5+} doping can improve conductivity, V_{OC} and light absorption [151].

4.4 Transition metals

The incorporation of transition metals into TiO_2 gives rise to the formation of a wide range of new energy levels close to the CB arising from their partially filled d -orbitals. This makes transition metals suitable materials to tune the CB structure. The transition metals discussed here are scandium [152], vanadium [153–155], chromium [83,156–159], manganese [160–162], iron [163,164], cobalt [160,162], nickel [165–167], copper [162,168,169], zinc [90,126,130,161,170–178], yttrium [179–181], zirconium [102,140,182–184], niobium [44,60,70,71,102,154,185–191], molybdenum [166], silver [192], tantalum [43,59,154,193–197] and tungsten [64,81,174,198–202].

4.4.1 Scandium

Sc^{3+} is an interesting dopant because of its similar size compared to Ti^{4+} . It creates a 'solid solution', where Sc^{3+} embedding gives rise to defect sites. Synchrotron scattering measurements showed substitutional incorporation of Sc^{3+} with a minimal distortion of the TiO_2 -lattice. BET and pore size and volume analysis (BJH) showed surface area and porosity were not affected in the relevant concentration range and dye adsorption was unchanged. V_{FB} was shifted negatively (Figure 3b), which was confirmed by widening of the band gap. This should result in a V_{OC} increase, but lower J_{SC} through reduction of electron injection. A lowering of V_{OC} was however observed, possibly due to an increase in series resistance. Carrier density and transport rate decreased, but electron lifetime increased, resulting in an increase in J_{SC} [152].

4.4.2 Vanadium

A gradient with decreasing V^{5+} doping was generated by the sequential deposition of differently doped TiO_2 nanoparticles, which enhanced electron transport. A gradual red shift in UV/Vis absorption spectra with increasing doping concentration indicated a positive shift in V_{FB} (Figure 3c). In the used device architecture the layered structure formed a graded pathway along which electrons can be transferred to the electrode (Figure 4). This led to an increase of the electron transfer rate and decreased recombination, leading to higher J_{SC} and V_{OC} [153]. The V_{FB} shift was also found in a different study through Mott-Schottky plots. IMPS and EIS showed an increase in transport rate which further enhanced J_{SC} [154,155].

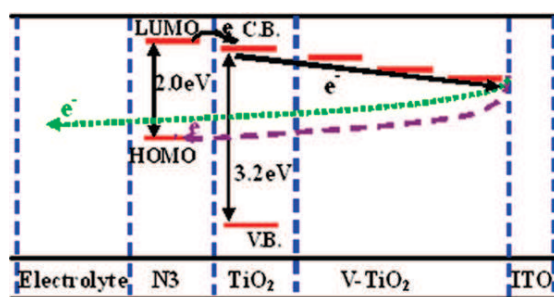


Figure 4: Schematic diagram of the energy levels for V-doped TiO_2 DSSCs, showing the gradient induced by the different V^{5+} doping levels. Reprinted with permission from [153]. Copyright 2011 American Chemical Society.

4.4.3 Chromium

Cr^{3+} doping of TiO_2 led to a clear red shift in the UV/Vis absorption spectrum, evidencing a decrease in band gap and VB shift, which resulted in a slightly lower value of V_{OC} . Although dye adsorption is not affected, Cr^{3+} doping seems to influence the TiO_2 crystal structure, as a clear rutile peak was detected in the XRD spectrum. EIS shows a decrease in charge transfer resistance and open-circuit voltage decay (OCVD), and an increase in electron lifetime, which led to higher values of J_{SC} . It was suggested that the reason for the better conductivity is an increase in free charges injected by Cr^{3+} doping [156].

For the high Cr^{3+} doping concentration of 3 at.% rutile formation was inhibited, but some brookite formed instead, and the dye adsorption was increased. The optical band gap was decreased, increasing electron injection efficient efficiency, at the expense of a V_{OC} reduction [157]. The exact role of mixed crystal phases remains poorly understood.

At very high Cr^{3+} doping concentrations of $\sim 10\%$, TiO_2 behaves as a p-type semiconductor, as confirmed by measuring the Hall effect. The introduction of Cr^{3+} into TiO_2 causes E_{F} to move towards the VB. This made it possible to construct a TiO_2 based p-n homojunction. Because of the diode like character, recombination is repressed, leading to an increase in J_{SC} and efficiency [158,159].

A high-throughput testing of dopants showed that Cr co-doped with Sb resulted in a massive increase in J_{SC} and a small decrease in V_{OC} . It is suggested that this is caused by an electron trans-

fer from Sb to Cr, which prevents the formation of oxygen vacancies and Ti^{3+} species [83].

4.4.4 Manganese

It was shown that Mn^{2+} doping can reduce particle size (XRD) and increase surface area (BET), but because of a positive shift of V_{FB} (Figure 3c) and the introduction of a large number of recombination sites due to a high doping concentration, V_{OC} , J_{SC} and efficiency decreased [160]. A separate study did not show a reduction in particle size. But because of the positive shift of V_{FB} , J_{SC} was enhanced, resulting in a slightly higher efficiency [161, 162].

4.4.5 Iron

Fe^{3+} -doping was reported to reduce the trap density and charge recombination, while improving dye adsorption, resulting in drastically improved values of J_{SC} [163].

At high concentrations ($\sim 10\%$) of Fe^{3+} , TiO_2 behaves as a p-type semiconductor. The introduction of Fe^{3+} into TiO_2 caused E_{F} to move towards the VB. This made it possible to construct a TiO_2 based p-n homojunction. Because of the diode like character, recombination was reduced [164].

4.4.6 Cobalt

Cobalt doping of TiO_2 was shown to drastically deteriorate DSSC performance due to the formation of sub-band gap states that reduce V_{OC} and act as recombination centres, as evidenced by UV/Vis absorption spectroscopy and EIS [160, 162]. The used doping concentration in [160] was however rather high at 12.6 at.%. Doping at these high concentrations is likely to give rise to massive lattice distortions and accompanying defects. Low doping of 0.2 at.% in [162] showed a much more modest decrease in efficiency.

4.4.7 Nickel

Ni^{2+} -doping was shown to enhance the crystallinity of electrospun TiO_2 nanowires, enhancing charge mobility. A Mott-Schottky plot showed a negative shift of V_{FB} (Figure 3b), which in combination with reduced recombination leads to improved V_{OC} [165].

Separate studies found that Ni^{2+} doping decreased particle size, resulting in an increase in J_{SC} . The decreased band gap indicates a positive shift of V_{FB} (Figure 3c). The V_{OC} loss

was compensated by a reduced recombination rate [166, 167].

4.4.8 Copper

Surface doping of TiO_2 with Cu^{2+} drastically increased both J_{SC} and V_{OC} . The increase in V_{OC} is caused by a negative shift of V_{FB} (Figure 3b) due to the interaction of Cu^{2+} with defect states. OCVD showed that recombination was suppressed resulting in improved J_{SC} . Cu^{2+} doping also seems to improve the electron transfer from the dye to the electron conductor by providing an alternative route for electrons from the dye into TiO_2 [168].

Other studies confirmed the negative shift of V_{FB} and showed a similar increase in V_{OC} . Despite an increase in adsorption, J_{SC} decreased drastically, caused by less efficient electron injection and a redox reaction of Cu with the electrolyte [162, 169].

4.4.9 Zinc

Because of the similar ion sizes of Ti^{4+} and Zn^{2+} , lattice distortion is small when inserting Zn^{2+} into the TiO_2 -lattice, which was confirmed by XRD. Zn^{2+} -doping was shown to increase both J_{SC} and V_{OC} [170]. V_{FB} was negatively shifted (Figure 3b), while recombination increased, resulting in a slight increase in V_{OC} . The electron density and transport rate were increased, leading to higher values of J_{SC} [171, 172]. By reducing recombination and increasing surface area and dye adsorption a massive increase in efficiency could be achieved [173, 174], but the negative shift of V_{FB} can lead to severely decreased electron injection and J_{SC} [175].

In contrast, other studies reported a positively shifted V_{FB} (Figure 3c) and reduced recombination, while electron densities and transport were increased as well [90, 126, 130, 161, 176, 178]. Zn^{2+} doping was also shown to inhibit the anatase-rutile phase transformation, increasing device performance [177].

The discrepancy in V_{FB} shift can be explained by the close proximity of the CB of ZnO and TiO_2 [203]. Slight variations in synthesis protocols might result in the Zn^{2+} impurity energies being either below or above the CB of TiO_2 , resulting in a positive or negative shift of V_{FB} respectively.

4.4.10 Yttrium

Previous studies have shown that Y^{3+} -doping does not affect the optical band gap [41], which suggests that J_{SC} could be improved without suffering a loss in V_{OC} . Mott-Schottky plots showed that Y^{3+} -doping can negatively shift V_{FB} (Figure 3b) leading to improved values of V_{OC} . In addition J_{SC} was significantly enhanced, which was attributed to up-conversion. Incident Photon to Current Efficiency (IPCE) however showed an improvement for the entire optical spectrum which suggests additional effects play a role in improving J_{SC} [179, 180].

In another study the interstitial incorporation of Y^{3+} into the TiO_2 -lattice was confirmed by XRD. The surface area of mesoporous assemblies was slightly increased, increasing dye adsorption. Contrary to previous literature, UV/Vis absorption spectroscopy showed a marked decrease of the band gap and an increase in conductivity. Charge extraction measurements showed no change in trap density and the energy distribution below the CB. Photovoltage decay measurements showed an increase in electron lifetime, but this comes at a loss in the transport rate. The increase in V_{OC} seems to be a result of a reduction in recombination, compensating the positive V_{FB} shift (Figure 3c). J_{SC} increased due to better electron injection and collection efficiencies. In addition, no TiCl_4 treatment of the TiO_2 scaffold was needed simplifying device manufacture [181].

4.4.11 Zirconium

The CB of ZrO_2 is located ~ 0.7 eV above the CB of TiO_2 . From this it can be expected that doping TiO_2 with Zr^{4+} will shift the CB upwards.

Zr^{4+} -doping proved to decrease particle size, resulting in an increased surface area of nanoparticle assemblies and dye adsorption. The band gap was indeed found to be increased, indicating a negative shift of V_{FB} (Figure 3b). These factors contributed to increased values of J_{SC} and V_{OC} [182]. Additional research found that the recombination rate was hardly affected and that the improved V_{OC} was purely caused by the CB shift [183]. Other studies reported much higher [102, 184], or lower recombination rates upon doping [140].

4.4.12 Niobium

Niobium is probably the most studied cationic dopant for TiO_2 in DSSCs because of promising optical and electronic properties [204]. Even for

this well studied system, there are some discrepancies between different reports, which indicates that the effect of the doping is strongly dependent on the type of defects induced by the TiO_2 synthesis method.

Initial attempts were not very successful as a positive shift of V_{FB} (Figure 3c) and a decrease in dye adsorption led to poor device efficiencies [102], although charge mobility was increased [185].

In further studies a Nb^{5+} doped HBL deposited via pulsed laser deposition showed an increase in J_{SC} , but a minute loss in V_{OC} . EIS showed slightly more current leakage for the doped compact layer, leading to a lower V_{OC} . But in addition the resistivity between the HBL and mesoporous TiO_2 dropped, leading to more efficient electron transfer between the two layers and thus a higher J_{SC} [70]. Optimization of the deposition protocol prevented leakage and led to an increase in V_{OC} [71].

A novel water soluble Nb^{5+} -precursor made it possible to evenly distribute Nb^{5+} ions throughout anatase TiO_2 , resulting in more efficient devices. XRD showed an increase in crystallite size, but dye adsorption remained largely unchanged, indicating that the particle size was not affected. This means there are less grain boundaries in the material, or the particles were bigger and Nb^{5+} increased the dye concentration [205], improving in both cases the conductivity of the material. UV/Vis absorption showed a decreased band gap and positively shifted V_{FB} , resulting in more efficient electron injection at the expense of a lower V_{OC} . EIS confirmed the drop in resistivity between TiO_2 particles and showed that doping reduced recombination, in part compensating the loss in V_{OC} by the shift of V_{FB} [186]. Another study showed a positive shift of V_{FB} by a Mott-Schottky plot and an increased transport rate by IMPS [154], resulting in lower a V_{OC} but higher J_{SC} .

A similar trend was found for devices doped with 2.5 mol% Nb^{5+} . Interestingly, V_{OC} increased for these low concentrations, caused by a decrease of oxygen vacancies and recombination. As the doping concentration increases, the CB is lowered, enhancing electron injection and J_{SC} [187]. EIS showed an increase in electron lifetime at low concentrations, but for higher doping concentrations shorter electron lifetimes were observed. This explains the observed V_{OC} trend. The transport rate was increased leading to a higher J_{SC} [188]. It was found that the drop in V_{OC} could be prevented by adding a hole conductor co-adsorbant, which dras-

tically decreased recombination [189].

It also proved to be possible to prevent a loss in V_{OC} by lowering the doping concentration (< 0.5 mol%). Smaller particles and larger a surface area led to increased dye adsorption. Charge extraction measurements showed a downward shift of the trap states, lowering the CB and V_{OC} . Transient studies showed longer electron lifetimes, but a lower transport rate, resulting in an overall higher charge collection efficiency. Reduced recombination compensated for the loss in V_{OC} due to the shifted CB, resulting in a device with better J_{SC} and V_{OC} , drastically improving efficiency [190]. Similar electronic properties were found for Nb^{5+} doped TiO_2 nanotubes [60] and rutile nanorods [44].

A recent study showed an increase in both J_{SC} and V_{OC} . A decrease in recombination was observed through EIS and transient photo current and is responsible for the improved V_{OC} [191].

These results seem to suggest that it is only possible to improve J_{SC} without negatively affecting V_{OC} when the TiO_2 is relatively defect free. In low-defect TiO_2 , a small amount of Nb^{5+} is needed to passivate oxygen defects and reduce recombination. This implies that only few Nb^{5+} sub-band gap states are formed and the effect of these states on V_{OC} is compensated by a reduction in recombination, while they increase J_{SC} by enhancing electron injection. For lower quality TiO_2 much higher doping concentrations are needed to reduce recombination and improve electron injection, resulting in more sub-band gap states, which lowers V_{OC} more than can be compensated through recombination suppression.

4.4.13 Molybdenum

Mo^{6+} -doping proved to effectively decrease particle size (XRD) and band gap (UV/Vis absorption). Due to the increased surface area, an increase in J_{SC} was observed. Although a V_{OC} loss might be expected as a result of the smaller band gap, the reduced recombination rate resulted in a much enhanced V_{OC} [166].

4.4.14 Silver

Calculations have predicted that doping with Ag^+ can heavily affect the optic and electronic properties of TiO_2 [206]. XRD evidenced the inhibition of rutile formation. Reduced charge transfer resistance due to enhanced charge transport results in higher J_{SC} . Increased charge lifetime indicates re-

combination is suppressed, resulting in higher V_{OC} (EIS) [192].

4.4.15 Tantalum

XRD showed particle size was not affected by incorporation of Ta^{5+} . V_{FB} was shifted positively (Figure 3c), resulting in a lower V_{OC} but enhanced electron injection. The electron density and transport rate were also increased, leading to an improved J_{SC} [154, 193–195]. Interestingly, the opposite behaviour was found for Ta^{5+} doped rutile nanowires [43]. An explanation can be found in a different study where anodized Ta^{5+} -doped TiO_2 nanotubes were annealed at $450^\circ C$ and $550^\circ C$, inducing different defects and mixtures of crystal phases. The devices annealed at $450^\circ C$ showed characteristics similar to [193], whereas the devices annealed at $550^\circ C$ contained a larger fraction of rutile and characteristics were more similar to [43] suggesting the difference is largely caused by the rutile content [197]. The CB of rutile has been reported to be approximately 0.2 V lower than the CB of anatase [207]. When Ta^{5+} induces defects in this 0.2 V wide range it will have opposite effects on the electronic properties. This is probably also true for anatase TiO_2 that is synthesized by different methods and as a result has a different distribution of defect states, varying the position of CB.

Other studies found both J_{SC} and V_{OC} were increased, which was attributed to increased dye adsorption [196], Mott-Schottky plots showed a negative shift of V_{FB} (Figure 3b). V_{OC} was further enhanced by suppressed recombination (EIS, IMVS) [59, 197].

4.4.16 Tungsten

XRD showed W^{6+} insertion results in smaller particles and thus mesoporous assemblies with bigger surface areas. An increase in J_{SC} was found, although dye adsorption was unchanged. The electron lifetime was greatly enhanced indicating a reduction in recombination [81, 174]. A more detailed study shows a similar trend in device performance. V_{FB} was shown to be positively shifted (Figure 3c), improving electron injection but at the cost of lowering V_{OC} . IMPS showed a decrease in electron diffusion, IMVS an increase in electron lifetime and thus a decrease in recombination, compensating for the lower CB [198]. This was further confirmed by DFT calculations [199], EIS [200, 201] and OCVD [202].

One study reported a blue shift of the absorption band edge (UV/Vis absorption) for electrospun nanowires, indicating a negative shift in V_{FB} (Figure 3b), which in combination with longer electron lifetimes lead to a marked increase in V_{OC} . An increase in dye adsorption caused J_{SC} to improve as well [64].

4.5 Post-transition metals

In the periodic table the post-transition metals are located between the transition metals and the metalloids. As such, post-transition metals have some non-metal properties, showing covalent bonding effects. The investigated post-transition metals are aluminum [51, 80, 81, 208–210], gallium [181], indium [83, 211] and tin [73, 78, 83, 147].

4.5.1 Aluminum

Aluminum is a group III metal with good optical quality, low resistivity and high conductance [212]. This makes Al^{3+} an interesting candidate for doping.

In Al^{3+} doped TiO_2 improved values of V_{OC} were reported, with largely unaffected J_{SC} . XPS studies showed a decrease in Ti^{3+} defects, which was accompanied by a decrease in recombination. This resulted in a higher V_{OC} , but reduced J_{SC} . Higher dye loading in mesoporous Al^{3+} -doped TiO_2 compensated this loss and photo currents for doped and undoped samples were comparable [81]. The increase in V_{OC} might also be caused by a negative shift of V_{FB} (Figure 3b) as was evidenced by UV/Vis absorption spectroscopy [208]. A decrease in the number of trap states was also shown by photo-thermal deflection spectroscopy (PDS). Additionally it was shown that by decreasing the number of trap states the device is much less sensitive to UV instigated oxygen desorption, leading to significantly longer device lifetimes [51]. Another study found that V_{FB} was slightly negatively shifted upon Al^{3+} -doping due to an increase in trap density, but this was compensated by an increase in current caused by longer electron lifetimes. XPS studies showed no change in the Ti^{3+} concentration with Al^{3+} -doping. In this study there is no clear evidence that Al^{3+} dopes into the TiO_2 -lattice. It is more likely that islands of Al_2O_3 were formed on the TiO_2 surface, which may act as a blocking layer, increasing electron lifetime [80]. For 20% Al^{3+} doped TiO_2 it was found that Al^{3+} substituted both into the TiO_2 -lattice and formed a separate Al_2O_3 phase. Sub-

stitutional Al^{3+} eliminated deep traps by substituting Ti^{3+} , resulting in a higher V_{OC} . A larger surface area of the mesoporous electrode and better charge injection resulted in a larger J_{SC} , while the Al_2O_3 phase acted as a blocking layer, preventing charge recombination [209].

Al -doping was shown to inhibit the formation of rutile, leading to a decreased band gap and enhancing J_{SC} through improved electron injection. A larger surface area of the nanoparticle assembly and higher anatase content further improved J_{SC} . Reduced recombination rate partially compensated the loss in V_{OC} due to the band gap reduction [210].

4.5.2 Gallium

Previous studies have shown that Ga^{3+} -doping does not affect the TiO_2 optical band gap [213], which suggests that J_{SC} can be improved without suffering a loss in V_{OC} .

The incorporation of Ga^{3+} into the TiO_2 -lattice was confirmed by XRD. A Rietveld analysis showed that Ga^{3+} substitutes Ti^{4+} in the TiO_2 -lattice. The surface area and porosity of nanoporous electrodes were slightly increased, allowing an increase in dye adsorption. XPS showed an increase in oxygen vacancies upon Ga^{3+} -doping. Despite the increase in oxygen vacancies, a drop in resistivity was measured. Charge extraction measurements showed no change in the trap density and energy distribution below the CB. Photovoltage decay measurements showed an increase in electron lifetime, but this came at a loss in the transport rate. The increase in V_{OC} seemed to be a result of a reduction in recombination, rather than a shift of the CB. In addition, no $TiCl_4$ treatment of the mesoporous scaffold was needed [181].

4.5.3 Indium

Although most studies focus on the doping of the mesoporous TiO_2 structure, doping of the HBL can also lead to a marked increase in performance. It was shown that the transmittance of a In^{3+} -doped HBL was higher than that of pristine TiO_2 . This allows more photons into the active layer, leading to an increase in absorption and J_{SC} . The observed negative shift in V_{FB} (Figure 3b) of the HBL will also result in a shift in V_{FB} of the mesoporous TiO_2 , leading to a higher V_{OC} . A decrease in dark current and a higher onset potential is an indication that the In^{3+} doped HBL prevents re-

combination more effectively, which is supported by a longer electron lifetime as measured by EIS and OCVD. The V_{FB} shift and reduced recombination led to a higher V_{OC} [211].

A high throughput screening of 35 elements showed that In^{3+} was one of the most promising dopants (along with Sb and Sn). This study similarly found a negative shift for V_{FB} [83].

4.5.4 Tin

The particle size and dye adsorption were not affected by Sn^{4+} -doping. V_{FB} was negatively shifted (Figure 3b), resulting in an increase in V_{OC} , which was limited by increased recombination because the Sn^{4+} -ions acted as recombination centers. The increase in electron density and faster transport led to a higher electron collection efficiency and J_{SC} [73, 78, 83, 147].

4.6 Lanthanides

Because of their 4f bands, lanthanides provide interesting optic and electronic properties [214], such as up-conversion, photoluminescence or down-conversion [215, 216], making it possible to harvest photons that are outside the absorption region of most dyes (400-800 nm). Although there are some reports that show effective up- or down-conversion [216–218], these processes are not yet very efficient in DSCCs, and their exact role in improving device efficiencies is unclear. Because many optical conversion studies do not consider the effect of doping on the electron transport rate and lifetime, the exact contribution of conversion is hard to quantify. Lanthanides that have been used to dope TiO_2 are lanthanum [219–221], cerium [222, 223], neodymium [224], samarium [225, 226], europium [225, 227–230], erbium [229, 231–236], thulium [237, 238] and ytterbium [231, 232, 234–239].

4.6.1 Lanthanum

Lanthanum is an interesting element because of its high binding strength to oxygen. When La^{3+} is doped into TiO_2 , it will scavenge oxygen and induce vacancies on the surface [240]. XRD and BET analyses showed that the particle size and the mesoporous surface area were largely unaffected by doping, but the dye adsorption was significantly increased. This can be explained by an increase in oxygen vacancies, which has been reported to increase dye loading [75]. This theory has been confirmed by EPR analysis, which

showed a strong correlation between density of oxygen vacancies, dye loading and device efficiency [219, 220].

A post-treatment with an acidic La^{3+} solution was shown to drastically increase J_{SC} although no La^{3+} was detected in the final particles and no morphology change was observed. An increase in electron density, combined with a down-shifted CB and increased dye adsorption was responsible for the increase in J_{SC} [221].

4.6.2 Cerium

It is known that Ce induces unoccupied 4f states just under the TiO_2 CB [241]. This may enlarge the driving force for electron injection from the dye into TiO_2 .

The crystallite size and dye adsorption capability were not significantly changed upon doping. XPS showed that both Ce^{3+} and Ce^{4+} were present and the VB was unaffected. The UV/Vis absorption spectrum showed a red-shift, which indicated that Ce indeed induces unoccupied 4f states just under the TiO_2 CB. This was confirmed by cyclic voltammetry. Charge extraction and EIS measurements showed an increase in the electron density and capacitance due to enhanced electron injection, resulting in a higher J_{SC} , but caused a loss in V_{OC} [222]. A follow up study showed that the dopant acted solely as a surface trap state and therefore it was possible to counteract some of the adverse effects of Ce-doping by a $TiCl_4$ treatment [223].

4.6.3 Neodymium

UV/Vis absorption spectroscopy indicated narrowing of the band gap upon Nd^{3+} -doping. This suggests a downward shift of the CB, which would explain the reduced V_{OC} . The amount of adsorbed dye was unaffected, but due to enhanced electron injection and reduced recombination, J_{SC} saw a marked increase [224].

4.6.4 Samarium

Sm^{3+} -doping decreased the anatase particle size and increased dye adsorption. In combination with down-conversion this led to an improved J_{SC} [225]. Another study showed an additional improvement in V_{OC} , which was suggested to be the result of p-type doping and recombination reduction [226].

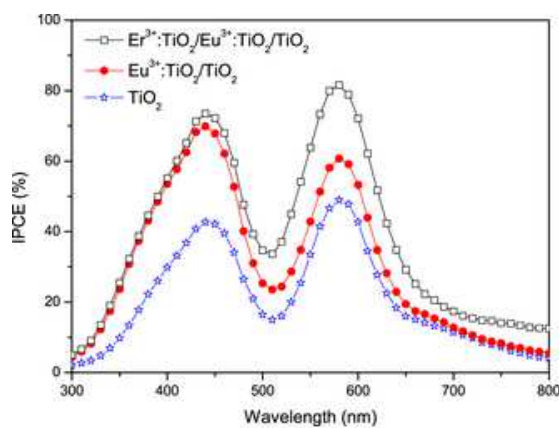


Figure 5: IPCE of $\text{Eu}^{3+}/\text{Er}^{3+}$ -doped TiO_2 DSSCs in light range of 300 – 800 nm. Although some of the increased IPCE above 700 nm can be ascribed to up-conversion, the drastic improvement for the whole spectrum suggests doping plays a more important role. Reprinted with permission from [229]. Copyright 2013 John Wiley & Sons, Inc.

4.6.5 Europium

Due to the 4f bands of Eu^{3+} it is possible to achieve down-conversion with Eu^{3+} doped TiO_2 [218]. A second important effect is a shift of the CB. It was found that dye adsorption increased upon doping. IPCE shows an absorption increase for the entire optical spectrum, with a new peak around 260 nm caused by down-conversion, leading to an increase in J_{SC} [225, 227]. Other studies reported a negative shift of V_{FB} (Figure 3b), leading to a higher V_{OC} [228–230].

4.6.6 Erbium

Er^{3+} has energy bands inside the band gap of TiO_2 which are expected to promote up-conversion. An increase in J_{SC} was found, which was attributed to up-conversion, but doping effects likely play a big role as the IPCE over the whole spectrum is increased (Figure 5). V_{OC} was increased due to a negative shift of V_{FB} (Figure 3b) [229, 231–234]. EIS showed a drop in resistivity, indicating an improvement in conductivity and reduced recombination, further contributing to enhanced values of J_{SC} and V_{OC} [235]. The absorption edge was found to be red-shifted indicating a downward shift of CB, although this was probably caused by the fluorine co-dopant [236].

4.6.7 Thulium

The observed up-conversion improved J_{SC} and an increase in V_{OC} suggested an upward shift of the CB [237, 238].

4.6.8 Ytterbium

No significant change in particle size was observed upon Yb^{3+} -doping. Dark current measurements show decreased recombination, which explains an increase in V_{OC} [239]. Later studies report that due to up-conversion, Yb^{3+} doping can enhance the J_{SC} . It was also suggested that the increased V_{OC} was due to a negative V_{FB} shift (Figure 3b) [231, 232, 234–238].

4.7 Summary

In short, doping can affect five different properties of anatase TiO_2 .

- *Flat-band potential.* V_{FB} can be shifted either positively or negatively; a positive shift is indicative of a downward shift of the CB and E_{F} while a negative V_{FB} shift indicates an upward shift of CB and E_{F} . A positive shift of V_{FB} makes electron injection easier, increasing J_{SC} . Because of a smaller difference between E_{F} of TiO_2 and the HTM V_{OC} is decreased. A negative shift of V_{FB} will have the opposite effect on J_{SC} and V_{OC} (Figure 3).
- *Recombination rate.* A decrease in the number of defect states usually enhances the electron lifetime and reduce recombination rate, resulting in an increase in V_{OC} . Because of the dependence on trap states for electron transport based on the trap-detrap mechanism, this can however lead to a decrease in electron mobility and J_{SC} .
- *Electron transport rate.* An increase in shallow trap states can lead to enhanced electron mobility and thus a higher J_{SC} . Simultaneously the introduced trap states can promote recombination which leads to a decreased V_{OC} (Figure 3).
- *Dye adsorption.* The dopant can change the growth rate of TiO_2 particles resulting in differently sized particles, affecting the amount of adsorbed dye and number of grain boundaries. Additionally, the dopant may affect dye adsorption by a change in binding affinity of the dye to the doped surface.

Dopant	Comments	V_{FB} pos.	V_{FB} neg.	Recombination	Transport	Absorption
Lithium			[85, 86]	[86]	[85]	
Magnesium			[89]			[89]
	Zn co-doped	[90]			[90]	
Calcium		[91–93]		[92, 93]	[91–93]	
Boron			[97]		[97]	
	nanotubes	[100]		[100]	[100]	
	N co-doped		[98, 99]	[98, 99]		
Silicon				[101]	[101]	
Germanium			[102]			[102]
Antimony		[103]			[103]	
	Cr co-doped	[83]		[83]	[83]	
	F co-doped			[147]	[147]	
Carbon		[99, 106, 107]		[99, 107]	[99, 107]	
Nitrogen		[99, 107–117]		[133–143]	[107, 125–127]	[108–117]
		[119, 121]			[129–132]	[119, 121]
		[123–127]				
		[129–142]				
	S co-doped	[82, 118]				[82, 118]
		[120, 128]				[120, 128]
	B co-doped		[98, 99]	[98, 99]		
	solid HTM	[122]				[122]
Fluorine		[141]		[99, 141]	[145, 147]	
				[146, 147]		
	Nb/Sn/Sb/Ta co-doped			[147]	[147]	
	Er co-doped	[236]				
	HBL				[144]	
Sulphur	N co-doped	[82, 118]				[82, 118]
		[120, 128]				[120, 128]
Iodine		[148]		[148]		
Scandium			[152]	[152]		
Vanadium		[153–155]		[153]	[153–155]	
Chromium		[156, 157]		[156, 158, 159]	[156]	[157]
	Sb co-doped	[83]		[83]	[83]	
Manganese		[161, 162]				[160]
Iron				[163, 164]		[163]
Cobalt	detrimental					
Nickel		[166, 167]		[166, 167]		[166, 167]
	nanowires		[165]	[165]	[165]	
Copper			[162, 168, 169]	[168]	[168]	[162, 169]
Zinc		[126, 130, 161]	[172–175]	[173, 174]	[126, 130]	[173, 174, 177]
		[176, 178]			[161, 172]	
					[176, 178]	
	N co-doped		[171]		[171]	
	Mg co-doped	[90]			[90]	
Yttrium		[181]		[181]		[181]
	co-doped		[179, 180]			[179, 180]
Zirconium			[102, 140]	[140]		[182]
			[182–184]			

Niobium		[154, 186–188] [189–191]	[186, 187] [189–191]	[154, 185–189] [205] [70, 71]	[190]
	HBL nanotubes r-nanorods	[60] [44]	[60] [44]		
Molybdenum		[166]	[166]		[166]
Silver			[192]	[192]	
Tantalum		[154, 193–195]		[154, 193–195]	[196]
	FSP nanotubes r-nanowires		[59] [197] [43]	[59] [197] [43]	
Tungsten		[198]	[81, 174, 198] [200–202]		
	nanowires		[64]	[64]	[64]
Aluminum			[80, 208, 209]	[80, 81, 209]	[81, 209]
	phase stab. solid	[210]	[51]	[210]	[51]
Gallium				[181]	[181]
Indium			[83]		
	HBL		[211]	[211]	[211]
Tin			[73, 78, 83]	[73, 78, 83]	
	F co-doped			[147]	[147]
Lanthanum		[221]			[219–221]
Cerium				[222, 223]	
Neodymium		[224]		[224]	
Samarium				[226]	[225, 226]
Europium			[228–230]		[225, 227–230]
Erbium			[229, 231–234]	[235]	[229, 231–234]
	F co-doped	[236]			
Thulium			[237, 238]		[237, 238]
Ytterbium			[231, 232] [234–238]	[239]	[231, 232] [234–238]

Table 1: Dopants and their main contribution to the improvement of DSSCs.

- *Phase transition.* Doping can inhibit the anatase-to-rutile phase transition, reducing rutile instigated charge recombination.

The main contributions for improving TiO_2 properties in DSSCs are summarized for each element in Table 1. This illustrates that the doping of TiO_2 with the aim to improve DSSC performance is not trivial. The correct balance between the CB energy, charge transport and recombination rate has to be found to obtain an optimally working device. It is important that the energy levels introduced by the dopant are located close to the CB to prevent these levels from becoming recombination centers or causing a large negative shift in V_{FB} , inhibiting charge injection. The best results are obtained for TiO_2 with few deep trap states.

In this case, the properties of TiO_2 can be further improved by low-concentration doping, preventing the dopant from causing new trap states that give rise to detrimental effects such as increased recombination or decreased electron injection.

Because of the strong dependence of TiO_2 electronic properties on the fabrication protocol it is difficult to compare the effect of different dopants. This complicates the choice of dopant, particularly since opposite changes in device properties were found in many studies, employing the same dopant. For the moment, this means that for each synthesis method the ideal dopant and doping concentration has to be found by trial and error. High-throughput methods can be of significant help here, drastically cutting back the time needed to optimize each system [83].

5 Outlook: Perovskite Solar Cells

With the recent emergence of perovskite solar cells (PSCs) it will be interesting to see which lessons can be learned from DSSCs. Due to the high optical density and charge transport of perovskites, much thinner devices can be constructed and the influence of TiO_2 surface area is much reduced. Because of the instability of perovskite in liquid electrolytes [22] only solid HTMs are used. The high charge transport through the perovskite allows the construction of devices without mesoporous layer [11], but it is presently difficult to produce a pinhole free films [242], limiting device performance. Mesoporous structures help wetting of the substrate and prevent the formation of pinholes [12, 13]. Similar to DSSCs, most PSCs rely on a hole blocking layer of TiO_2 [10]. This implies that the electronic properties of TiO_2 are also important, both as compact and mesoporous layers, and similar to dye-sensitised solar cells doping will be important for performance enhancements in PSCs. So far, Mg [243], Nb [244, 245], Y [246, 247], Al [51] and Zr [248] doping of TiO_2 have been employed in perovskite solar cells.

Similar to Mg-doping in DSSCs [87–89], V_{OC} was improved in PSCs with a Mg-doped HBL, due to a higher CB energy and reduced recombination [243]. Nb-doping resulted in improved electron injection and transport, resulting in higher J_{SC} [244, 245].

In the case of Y-doping a small negative shift of V_{FB} was observed and recombination is slightly reduced. The main reason for the improvement in device performance was increased perovskite loading, leading to a marked increase in J_{SC} [246]. A separate study found increased electron transport led to higher J_{SC} for a planar device with doped HBL [247].

Al-doping was shown to reduce the number of oxygen vacancies and the associated deep trap states, effectively reducing recombination and increasing conductivity of the film. This led to an overall increase in J_{SC} . Additionally, it was shown that the long-term stability in inert atmosphere was significantly enhanced. This was ascribed to the elimination of oxygen defects by Al-doping. UV radiation causes the desorption of oxygen and in an inert atmosphere, where adsorbed oxygen can not be replenished, this leads to the emergence of oxygen vacancies that act as deep trap states, deteriorating device performance (Figure 6). By

reducing the number of traps through Al-doping this deterioration effect is much less profound [51].

A major problem in PSCs is hysteresis; the performance of the device depends strongly on how the measurement is performed. Typically the performance is much better sweeping from high to low voltages (forward bias) than vice versa, making it difficult to define the true power conversion efficiency. The precise mechanism causing hysteresis is yet unknown, although there are several hypotheses on the origin of hysteresis, such as the ferroelectric polarization [21, 249, 250], ion migration [21, 251] or deep trap states [21]. Trap states at the interface of perovskite and charge conducting material may play an important role. These trap states get filled under forward bias measurements, resulting in good contacts and high efficiency devices. Under short-circuit conditions the traps may empty, resulting in a poor device performance until the trap states are filled again [21, 251–255]. It was shown that by passivating interfacial traps, hysteresis could be drastically reduced, while overall device performance was improved [256]. By doping TiO_2 with Zr^{4+} hysteresis was decreased, while at the same time the CB was shifted upward and recombination was decreased, leading to an increase in V_{OC} [248]. This result suggests that doping can play an important role by decreasing surface trap states and reducing hysteresis.

Overall, it is likely that doping of TiO_2 may play an important role in improving efficiencies of PSCs. Doping can shift the CB, increase charge transport and reduce recombination. In addition, it may prolong device lifetimes, increase perovskite loading and play an important role in reducing hysteresis.

6 Techniques

There are several techniques that can give information on the effects of doping on the structural and electronic properties of TiO_2 . This section discusses the most common techniques and the information that can be extracted from the measurements.

6.1 Computational modelling

Computational modelling can be used to predict and design material properties. Density functional theory (DFT) has become a popular method due to its low computational cost, making it possible to quickly screen dopants for their suitability to

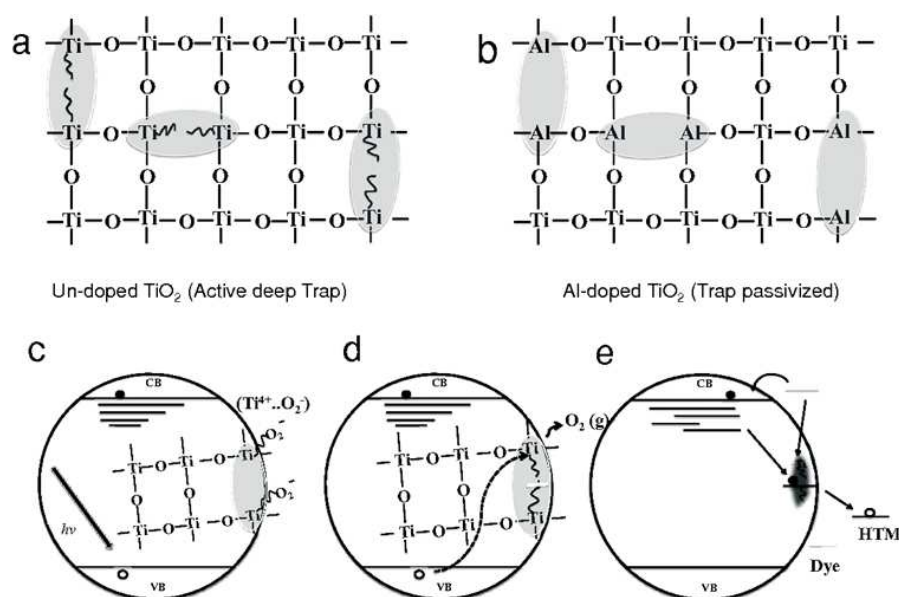


Figure 6: Schematic of Ti(III) trap passivation, doping and oxygen adsorption. (a) Oxygen defects in the lattice give rise to Ti(III) defects that form deep electronic traps. (b) Al substitution at the Ti(III) sites passivates these defects. (c) In the presence of oxygen, ionisation of Ti(III) gives rise to O² superoxide which passivates the trap sites. (d) Photoexcited holes neutralise and desorb O₂, activating Ti(III), which (e) enables charge recombination. Reprinted with permission from [51]. Copyright 2014 John Wiley & Sons, Inc.

increase TiO₂ properties [151,199]. However, caution must be taken as the band gap is often underestimated, leading to inaccurate predictions [257].

6.2 Morphological studies

To gain insight in the structure of (doped) TiO₂ several techniques can be employed. Electron microscopy offers the possibility to image nanostructures, from X-ray diffraction average particle size and dopant distribution can be determined and surface analysis quantifies the effect of doping on surface area and dye adsorption.

6.2.1 Electron Microscopy

Electron microscopy makes it possible to visualize and characterize nanostructures. Scanning electron microscopy (SEM) is generally used to study the surface topography and to measure the average particle size and film thickness. The latter can also be measured by a profilometer. If equipped with an energy dispersive X-ray (EDX) spectrometer, the distribution of elements in the film can also be mapped. Transmission electron microscopy (TEM) yields a higher resolution than SEM, but requires extremely thin samples, which makes TEM less well suited for topographic inves-

tigations. Atomic resolution allows to image the TiO₂ lattice and typically gives a better measurement of the average crystallite size.

6.2.2 X-ray diffraction

X-ray diffraction (XRD) is a precise method to determine the crystal structure of TiO₂. It is routinely used to determine the crystal structure and the presence of impurity phases. A typical XRD spectrum of anatase TiO₂ is shown in Figure 7 with the Miller indices (*hkl*) of the different peaks. The Rietveld refinement method allows a more detailed analysis of XRD spectra by using a least squares fit to approximate the measured profile [258]. This way it is possible to determine the average crystallite size *D* by using the Scherrer formula [259, 260]

$$D = \frac{K\lambda}{\beta \cos \theta}, \quad (4)$$

where *K* is a dimensionless shape factor which is dependent on the shape of the particle (0.9 for spherical particles), λ is the wavelength of the X-rays, β is the full width half-maximum (FWHM) after subtracting the instrumental line broadening and θ is the Bragg angle. It is important to

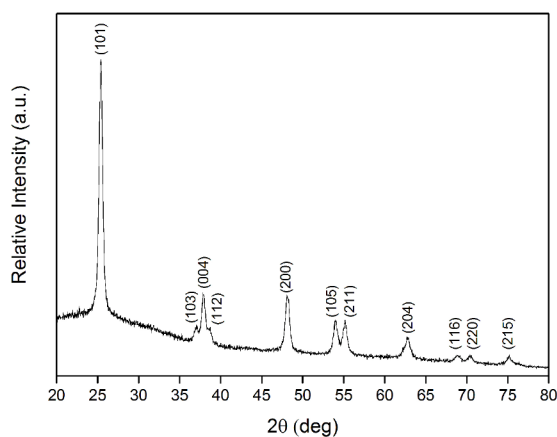


Figure 7: X-ray diffraction spectrum of anatase TiO_2 . Each peak is labeled with the corresponding Miller indices (hkl).

note that β and θ are in radians, whereas the instrumental output is usually in degrees. Furthermore, the inter-planar spacing d_{hkl} can be calculated with Bragg's law [261]

$$d = \frac{\lambda}{2 \sin \theta} \quad (5)$$

and using this interplanar spacing the lattice parameters a and c can be calculated using the Bragg formula for a tetragonal ($a = b$) lattice [162]

$$\frac{1}{d^2} = \frac{h^2 + k^2}{a^2} + \frac{l^2}{c^2}. \quad (6)$$

The change of the individual lattice parameters on doping can be determined by calculating the distortion degree of the lattice using [262]

$$R = \frac{2a\sqrt{2/3}}{c}. \quad (7)$$

Vegard's law provides an empirical method to assess the successful incorporation of a dopant. It states that there is a linear relation between the lattice distortion and the concentration of dopant. It requires that the crystal retains its lattice structure and the dopant and matrix form a solid solution [263].

6.2.3 Dye adsorption

The amount of dye adsorbed on the TiO_2 surface is typically a good measure to determine how many photons will be absorbed. Dye adsorption depends on the porosity of the mesoporous TiO_2 , which can be measured by gas adsorption. Gas adsorption isotherms are typically analyzed by the

Brunauer-Emmett-Teller (BET) theory [264] that yields the specific surface area of the material or by the Barrett-Joyner-Halenda (BJH) [265] analysis, which yields the pore size distribution. Doping however often affects the adsorption of the dye to TiO_2 (i.e. the dye affinity) implying differing the amounts of adsorbed dye for samples with the same surface area. In a more direct measurement, the dye can be desorbed from TiO_2 using a non-reactive solvent. By comparing the UV-vis absorption of the extracted solvent to reference spectra, the amount of adsorbed dye can be estimated. A combination of the two methods can be used to calculate the average dye density.

6.3 Spectroscopic techniques

By studying the interaction between light and matter the electronic structure of the material can be determined. The band gap, presence of defect states and material composition can be found through these methods.

6.3.1 UV/Vis spectroscopy

The main use for UV/Vis spectroscopy in TiO_2 doping studies is to obtain the direct and indirect band gap by determining the position of the absorption band edge. Absorption and reflectance are recorded in the range of 300-800 nm. Absorption and the direct band gap E_g are related through [266]

$$\alpha E = C(E - E_g)^{1/2}, \quad (8)$$

where α is the absorption coefficient, E the photon energy and C a proportionality constant. Sample reflectance can be converted to the Kubelka-Munk function [267], which is equivalent to the absorption coefficient in Equation (8)

$$F(R) = \frac{(1 - R)^2}{2R}. \quad (9)$$

Using a Tauc plot (Figure 8) [89, 268] it is possible to extract the direct and indirect band gap. In a Tauc plot $(F(R)E)^{1/r}$ is plotted versus E , where $r = \frac{1}{2}$ for the direct band gap and $r = 2$ for the indirect band gap. Extrapolation of the linear regime gives the band gap energy.

6.3.2 X-ray photoelectron spectroscopy

In X-ray photoelectron spectroscopy (XPS) the sample is irradiated with X-rays and the number

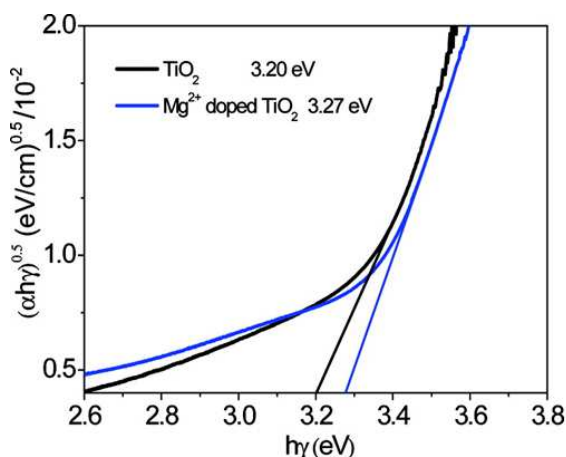


Figure 8: Determination of the indirect band gap energy for a TiO_2 film and a Mg^{2+} -doped TiO_2 film from the plot of $(\alpha E)^{1/2}$ versus the excitation energy, $h\gamma$ (α is the absorption coefficient, E is $h\gamma$, h is Planck's constant, and γ is the photon frequency). The indirect band gap energy is given by the intersect of the extrapolated linear regime with the x-axis. Reprinted with permission from [89]. Copyright 2011 American Chemical Society.

of escaping electrons and their energy are measured to gain information about the elemental composition and electronic state of the elements. For example, it is possible to quantify the amount of dopant in the sample and the Ti^{3+} to Ti^{4+} ratio [81].

6.3.3 FTIR spectroscopy

Fourier transform infrared (FTIR) spectroscopy measures optical absorption in a wide spectral range ($\sim 400\text{--}4000\text{ cm}^{-1}$) and gives information about atomic bond vibrations. The intensity and position of the peaks of stretching vibrations of Ti-O-Ti and Ti-O bonds give information about the interaction between TiO_2 and the dopant since they are related to the number and strength of Ti-O bonds. By doping into interstitial sites the dopant directly decreases the number of Ti-O bonds. The size, electron affinity and valency of the dopant also influences the strength and orientation of neighbouring Ti-O bonds.

6.3.4 Raman spectroscopy

Raman spectroscopy is used to find rotational, vibrational and other low-frequency modes in a system. A laser beam interacts with these samples modes, resulting in an up- or down-shift of the

photon energy. Each material has a distinct spectrum which allows the identification of impurity phases. Dopants alter the modes and in this way it is possible to measure the effect of the dopant on the TiO_2 crystal lattice. Raman spectroscopy is particularly useful to detect the formation of oxygen vacancies [269].

6.3.5 Material composition

Several methods are able to determine the amount of dopant in TiO_2 with great precision such as EDX spectroscopy [169], XPS spectroscopy [81], mass spectroscopy [187] or neutron activation analysis [270], which make use of unique “fingerprint” measurement spectra obtained upon sample irradiation.

6.4 Electromagnetic measurements

The interaction between magnetic fields and free charges in the sample makes it possible to determine the type of conduction, carrier concentration and detect trap states.

6.4.1 Hall effect measurement

When a magnetic field is applied on a current-carrying semiconductor, the charge carriers experience a force perpendicular to the magnetic field and the current. This is called the Hall effect, by measuring the strength of this effect the type of conduction (p- or n-type) and the carrier concentration are determined [271, 272].

6.4.2 Electron paramagnetic resonance analysis

In electron paramagnetic resonance analysis (EPR) the spins of unpaired electrons are excited by microwave radiation in a magnetic field. This makes it possible to detect trapped electrons, which are unpaired, and the corresponding trap states [220, 273]. The technique is similar to nuclear magnetic resonance analysis (NMR) with the exception that in NMR nuclear spins are excited.

6.5 (Photo-)Electrochemical measurements

By simulating real world conditions the performance of the solar cell can be predicted through the determination of the photovoltaic properties such as short circuit current density J_{SC} , open circuit voltage V_{OC} and fill factor FF .

A wide range of measurements where the sample is subjected to periodic optical or electronic perturbations provide information about the concentration, diffusion length and lifetime of electrons, CB position, density of trap states as well as transport and recombination processes. They include transient and decay measurements, electrochemical impedance spectroscopy (EIS), intensity modulated photo current spectroscopy (IMPS), intensity modulated photovoltage spectroscopy (IMVS) and open circuit voltage decay (OCVD) [9,274].

6.5.1 Photovoltaic properties

The power conversion efficiency of a solar cell is determined by measuring the current density as a function of applied voltage characteristics under illumination. The illumination spectrum and intensity should approximate that of the sun. To this end, a standardized light source of 100 mW/cm² AM 1.5 solar simulator is used. From the photo current-voltage (*I-V*) curve (Figure 9) J_{SC} , V_{OC} and FF are extracted. J_{SC} is the current in the absence of a net voltage, V_{OC} is the voltage in the absence of net current and FF is a measure for the "squareness" of the curve and is a good indication for the resistances in the device. FF is determined by dividing the maximum power output P_{max} of the device by $J_{SC} \times V_{OC}$. Parasitic resistances in the device lower FF ; for low voltages shunt resistances are dominating, while for high voltages the series resistance is important. These are revealed by *I-V* curves measured in the dark. Under dark conditions, a solar cell behaves as an ideal diode, and deviations from the ideal diode behaviour arise from injected current leakage.

The quantum efficiency is defined as the ratio of incident photons of a certain energy to the charges collected. The external quantum efficiency (*EQE*) considers all the incident photons including those that are transmitted and reflected, whereas internal quantum efficiency (*IQE*) only takes the absorbed photons into account. From this, a correlation between the energy of the photon and the probability of charge collection can be found.

Lastly, the stability of the device can be tested by measuring the device efficiency over a long period of time.

6.5.2 Electrochemical impedance spectroscopy

By perturbing an applied voltage with a small sine wave modulation the impedance can be

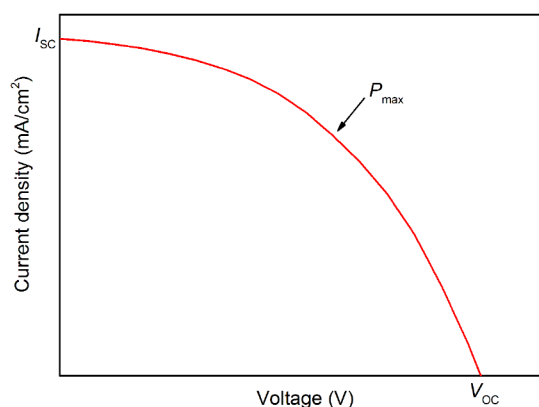


Figure 9: Typical *I-V* curve for DSSCs. Short circuit current density J_{SC} is given by the intersect with the y-axis and open circuit voltage V_{OC} by the intersect with the x-axis. Fill factor FF can be calculated from $\frac{P_{max}}{J_{SC} \times V_{OC}}$.

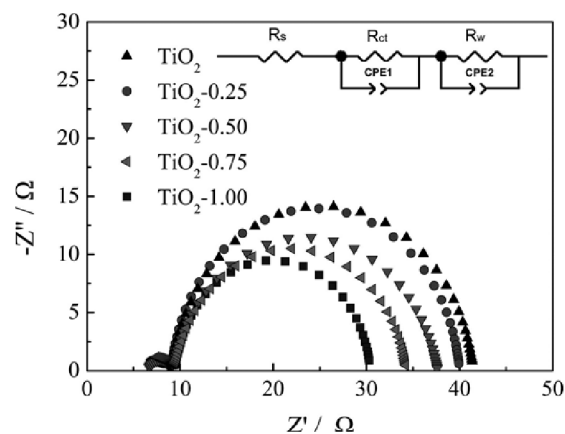


Figure 10: EIS spectra of TiO₂ and Sn-doped TiO₂ DSSCs. The inset shows the equivalent circuit that was used to find the electron lifetime and capacitance. Reprinted with permission from [73]. Copyright 2012 American Chemical Society.

found through the sinusoidal current response. Impedance can be defined as the frequency domain ratio of the voltage with respect to the current and is a complex value. The resulting function can be visualised with a Nyquist plot, where the real part of the function is plotted on the x-axis and the imaginary part on the y-axis. The system can be described by an equivalent circuit consisting of parallel and series connected elements (Figure 10). From this charge transfer and transport processes and capacitance can be extracted [9,274,275].

6.5.3 Electron transport

Because electron transport and recombination processes respond non-linearly to different light intensities they can be studied using a small perturbation of light modulated onto a higher constant light intensity. The output can again be visualised with a Nyquist plot. In IMPS a sinusoidal modulation of light intensity is applied and the photo current is measured as a function of this modulation [276]. The photo current response τ_{pc} depends on both the electron transport and recombination [54]. Under short-circuit conditions, the electron lifetime τ_n is usually much larger than the transport time τ_{tr} , implying $\tau_{pc} \approx \tau_{tr}$ [9].

The chemical diffusion coefficient D_n can be derived from the transport time

$$D_n = \frac{d^2}{C\tau_{tr}}, \quad (10)$$

where d is the thickness of the TiO_2 layer and C is a constant which depends on the absorption coefficient and direction of illumination [277].

6.5.4 Electron lifetime

The measurement of the electron lifetime is similar to the electron transport, but the open circuit potential rather than the photo current is measured. Under these conditions, photo-generated electrons are not extracted and will eventually recombine with holes. Using a small intensity modulation, the response time of the potential corresponds to the electron lifetime τ_n [278].

An alternative is the OCVD method, where V_{OC} is measured as a function of time after the light source is switched off [279]. The electron lifetime is calculated from the slope of the transient as

$$\tau_n = -\frac{kT}{e} \left(\frac{dV_{OC}}{dt} \right)^{-1}. \quad (11)$$

The advantage of this method is that the electron lifetime can be determined for a wide potential range in just one measurement.

A third method is time-dependent charge extraction [280], where the lifetime is given by

$$\tau_n = Q(t) \left(\frac{dQ(t)}{dt} \right)^{-1}. \quad (12)$$

$Q(t)$ is the extracted charge after decay in the dark for the time t , assuming recombination follows first-order kinetics.

IMVS and OCVD give similar values, while charge extraction usually gives a value that is

about 4 times higher [280]. This can be explained by the fact that the former methods are based on the recombination of photo induced excess charges, whereas the latter method gives an average lifetime for all the electrons in the TiO_2 [9].

6.5.5 Electron concentration

The electron concentration can be measured through charge extraction methods, where the current is integrated over time after the light has been switched off [281].

Alternatively the capacity is measured [282]. An open-circuit potential is established by a bias illumination after which a light pulse is applied. The resulting voltage rise is measured, while the transient photo current is measured separately under short-circuit conditions to calculate the injected charge. The capacity is given by the ratio of injected charge and voltage change.

Lastly, the electron concentration can be estimated from the slope of a Mott-Schottky plot (Section 6.5.6).

6.5.6 Flat-band potential

The flat-band potential V_{FB} can be derived from a Mott-Schottky plot, where the capacitance of the space charge region is measured as a function of voltage under depletion conditions. For a fit of the linear part of the curve, V_{FB} and electron density are given by the axis-intersect and the slope of the fit respectively (Figure 11) [193, 283]. The flat-band potential is usually referenced to a standardized electrode. A negative shift is indicative of an upward shift of CB, whereas a positive shift indicates a downward shift of CB.

6.5.7 Charge collection efficiency

The charge collection efficiency η_{CC} is an important parameter as it combines the results of electron transport and lifetime studies, enabling to find the ideal balance between the two. η_{CC} is given by [284]

$$\eta_{CC} = 1 - \frac{\tau_{pc}}{\tau_e} = \frac{1}{1 + \tau_{tr}/\tau_n}, \quad (13)$$

provided τ_{tr} and τ_n are measured at the same quasi-Fermi level.

A similar parameter is the electron diffusion length

$$L = \sqrt{D_n\tau_n}, \quad (14)$$

which is the average diffusion distance of electrons before they recombine with holes.

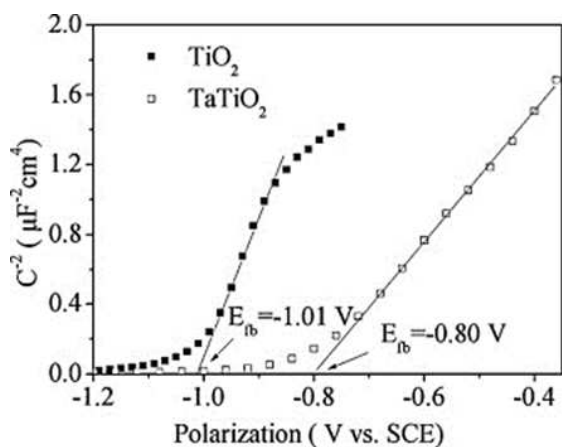


Figure 11: Mott-Schottky plots for TiO_2 and TaTiO_2 [193]. V_{FB} is given by the intersect of the extrapolated linear regime with the x-axis, the electron density by the slope. Reprinted with permission from [283]. Copyright 2007 American Chemical Society.

Acknowledgement

This work was supported by the Swiss National Science Foundation under the program NRP70 number 153990.

References

- [1] Grätzel, M. *Accounts of Chemical Research* **42**(11), 1788–1798 (2009).
- [2] Chu, S. and Majumdar, A. *Nature* **488**(7411), 294–303 (2012).
- [3] Lewis, N. S. and Nocera, D. G. *Proceedings of the National Academy of Sciences* **103**(43), 15729–15735 (2006).
- [4] Armaroli, N. and Balzani, V. *Angewandte Chemie International Edition* **46**(1-2), 52–66 (2007).
- [5] Lewis, N. S. *Science* **315**(5813), 798–801 (2007).
- [6] http://www.nrel.gov/ncpv/images/efficiency_chart.jpg.
- [7] O'Regan, B. and Grätzel, M. *Nature* **353**(6346), 737–740 (1991).
- [8] Snaith, H. J. and Schmidt-Mende, L. *Advanced Materials* **19**(20), 3187–3200 (2007).
- [9] Hagfeldt, A., Boschloo, G., Sun, L., Kloo, L., and Pettersson, H. *Chemical Reviews* **110**(11), 6595–6663 (2010).
- [10] Lee, M. M., Teuscher, J., Miyasaka, T., Murakami, T. N., and Snaith, H. J. *Science* **338**(6107), 643–647 (2012).
- [11] Liu, M., Johnston, M. B., and Snaith, H. J. *Nature* **501**(7467), 395–398 (2013).
- [12] Kim, H.-S., Lee, C.-R., Im, J.-H., Lee, K.-B., Moehl, T., Marchioro, A., Moon, S.-J., Humphry-Baker, R., Yum, J.-H., Moser, J. E., Grätzel, M., and Park, N.-G. *Sci. Rep.* **2** (2012).
- [13] Burschka, J., Pellet, N., Moon, S.-J., Humphry-Baker, R., Gao, P., Nazeeruddin, M. K., and Grätzel, M. *Nature* **499**(7458), 316–319 (2013).
- [14] Service, R. F. *Science* **344**(6183), 458 (2014).
- [15] Jeon, N. J., Noh, J. H., Kim, Y. C., Yang, W. S., Ryu, S., and Seok, S. I. *Nat Mater* **13**(9), 897–903 September (2014).
- [16] McGehee, M. D. *Nat Mater* **13**(9), 845–846 (2014).
- [17] Grätzel, M. *Nat Mater* **13**(9), 838–842 (2014).
- [18] Hao, F., Stoumpos, C. C., Cao, D. H., Chang, R. P. H., and Kanatzidis, M. G. *Nat Photon* **8**(6), 489–494 (2014).
- [19] Noel, N. K., Stranks, S. D., Abate, A., Wehrenfennig, C., Guarnera, S., Haghighirad, A.-A., Sadhanala, A., Eperon, G. E., Pathak, S. K., Johnston, M. B., Petrozza, A., Herz, L. M., and Snaith, H. J. *Energy Environ. Sci.* **7**, 3061–3068 (2014).
- [20] Mei, A., Li, X., Liu, L., Ku, Z., Liu, T., Rong, Y., Xu, M., Hu, M., Chen, J., Yang, Y., Grätzel, M., and Han, H. *Science* **345**(6194), 295–298 (2014).
- [21] Snaith, H. J., Abate, A., Ball, J. M., Eperon, G. E., Leijtens, T., Noel, N. K., Stranks, S. D., Wang, J. T.-W., Wojciechowski, K., and Zhang, W. *The Journal of Physical Chemistry Letters* **5**(9), 1511–1515 (2014).
- [22] Kojima, A., Teshima, K., Shirai, Y., and Miyasaka, T. *Journal of the American Chemical Society* **131**(17), 6050–6051 (2009).
- [23] Im, J.-H., Lee, C.-R., Lee, J.-W., Park, S.-W., and Park, N.-G. *Nanoscale* **3**(10), 4088–4093 (2011).
- [24] Wang, Z.-S., Kawauchi, H., Kashima, T., and Arakawa, H. *Coordination Chemistry Reviews* **248**(1314), 1381 – 1389 (2004). Michael Graetzel Festschrift, a tribute for his 60th Birthday, Dye Sensitized Solar Cells.
- [25] Mor, G. K., Varghese, O. K., Paulose, M., Shankar, K., and Grimes, C. A. *Solar Energy Materials and Solar Cells* **90**(14), 2011 – 2075 (2006).
- [26] Chen, X. and Mao, S. S. *Chemical Reviews* **107**(7), 2891–2959 (2007).
- [27] Leung, D., Fu, X., Wang, C., Ni, M., Leung, M., Wang, X., and Fu, X. *ChemSusChem* **3**(6), 681–694 (2010).
- [28] Rauf, M., Meetani, M., and Haindee, S. *Desalination* **276**(13), 13 – 27 (2011).
- [29] Park, H., Park, Y., Kim, W., and Choi, W. *Journal of Photochemistry and Photobiology C: Photochemistry Reviews* **15**(0), 1 – 20 (2013).
- [30] Chandiran, A. K., Nazeeruddin, M. K., and Grätzel, M. *Advanced Functional Materials* **24**(11), 1615–1623 (2014).
- [31] Kay, A. and Grätzel, M. *Chemistry of Materials* **14**(7), 2930–2935 (2002).
- [32] Qiu, Y., Chen, W., and Yang, S. *J. Mater. Chem.* **20**, 1001–1006 (2010).
- [33] Ko, S. H., Lee, D., Kang, H. W., Nam, K. H., Yeo, J. Y., Hong, S. J., Grigoropoulos, C. P., and Sung, H. J. *Nano Letters* **11**(2), 666–671 (2011).

- [34] Burnside, S., Moser, J.-E., Brooks, K., Grätzel, M., and Cahen, D. *The Journal of Physical Chemistry B* **103**(43), 9328–9332 (1999).
- [35] Nah, Y.-C., Paramasivam, I., and Schmuki, P. *ChemPhysChem* **11**(13), 2698–2713 (2010).
- [36] Banerjee, A. N. *Nanotechnology, Science and Applications* **4**, 35–65 (2011).
- [37] Li, G., Richter, C. P., Milot, R. L., Cai, L., Schmuttenmaer, C. A., Crabtree, R. H., Brudvig, G. W., and Batista, V. S. *Dalton Trans.*, 10078–10085 (2009).
- [38] Kim, B.-M., Rho, S.-G., and Kang, C.-H. *Journal of Nanoscience and Nanotechnology* **11**(2), 1515–1517 (2011).
- [39] Scanlon, D. O., Dunnill, C. W., Buckeridge, J., Shevlin, S. A., Logsdail, A. J., Woodley, S. M., Cawlow, C. R. A., Powell, M. J., Palgrave, R. G., Parkin, I. P., Watson, G. W., Keal, T. W., Sherwood, P., Walsh, A., and Sokol, A. A. *Nat Mater* **12**(9), 798–801 (2013).
- [40] Park, N.-G., van de Lagemaat, J., and Frank, A. J. *The Journal of Physical Chemistry B* **104**(38), 8989–8994 (2000).
- [41] Li, J., Yang, X., Yu, X., Xu, L., Kang, W., Yan, W., Gao, H., Liu, Z., and Guo, Y. *Applied Surface Science* **255**(6), 3731–3738 (2009).
- [42] Kim, H.-S., Lee, J.-W., Yantara, N., Boix, P. P., Kulkarni, S. A., Mhaisalkar, S., Grätzel, M., and Park, N.-G. *Nano Letters* **13**(6), 2412–2417 (2013).
- [43] Feng, X., Shankar, K., Paulose, M., and Grimes, C. *Angewandte Chemie* **121**(43), 8239–8242 (2009).
- [44] Yang, M., Ding, B., and Lee, J.-K. *Journal of Power Sources* **245**(0), 301–307 (2014).
- [45] Ardakani, H. *Thin Solid Films* **248**(2), 234–239 (1994).
- [46] Asahi, R., Taga, Y., Mannstadt, W., and Freeman, A. *Phys. Rev. B* **61**, 7459–7465 Mar (2000).
- [47] Paxton, A. and Thien-Nga, L. *Physical Review B (Condensed Matter and Materials Physics)* **57**(3), 1579–1584 (1998).
- [48] Sivaram, V., Crossland, E. J. W., Leijtens, T., Noel, N. K., Alexander-Webber, J., Docampo, P., and Snaith, H. J. *The Journal of Physical Chemistry C* **118**(4), 1821–1827 (2014).
- [49] Leijtens, T., Eperon, G. E., Pathak, S., Abate, A., Lee, M. M., and Snaith, H. J. *Nat Commun* **4**(2885) (2013).
- [50] Pathak, S. K., Abate, A., Leijtens, T., Hollman, D. J., Teuscher, J., Pazos, L., Docampo, P., Steiner, U., and Snaith, H. J. *Advanced Energy Materials* **4**(8), 1301667 (2014).
- [51] Pathak, S. K., Abate, A., Ruckdeschel, P., Roose, B., Gödel, K. C., Vaynzof, Y., Santhala, A., Watanabe, S.-I., Hollman, D. J., Noel, N., Sepe, A., Wiesner, U., Friend, R., Snaith, H. J., and Steiner, U. *Advanced Functional Materials* **24**(38), 6046–6055 (2014).
- [52] Bisquert, J. *The Journal of Physical Chemistry B* **108**(7), 2323–2332 (2004).
- [53] Adachi, M., Murata, Y., Takao, J., Jiu, J., Sakamoto, M., and Wang, F. *Journal of the American Chemical Society* **126**(45), 14943–14949 (2004).
- [54] Schlichthörl, G., Park, N. G., and Frank, A. J. *The Journal of Physical Chemistry B* **103**(5), 782–791 (1999).
- [55] Franco, G., Gehring, J., Peter, L. M., Ponomarev, E. A., and Uhlendorf, I. *The Journal of Physical Chemistry B* **103**(4), 692–698 (1999).
- [56] Kopidakis, N., Neale, N. R., Zhu, K., van de Lagemaat, J., and Frank, A. J. *Applied Physics Letters* **87**(20), – (2005).
- [57] Bisquert, J. and Vikhrenko, V. S. *The Journal of Physical Chemistry B* **108**(7), 2313–2322 (2004).
- [58] Radecka, M., Rekas, M., Trenczek-Zajac, A., and Zakrzewska, K. *Journal of Power Sources* **181**(1), 46–55 (2008).
- [59] Gu, F., Huang, W., Wang, S., Cheng, X., Hu, Y., and Lee, P. S. *Physical chemistry chemical physics : PCCP* **16**(47), 25679–83 (2014).
- [60] Yang, M., Kim, D., Jha, H., Lee, K., Paul, J., and Schmuki, P. *Chemical Communications* **47**(7), 2032–2034 (2011).
- [61] Peng, X. and Chen, A. *J. Mater. Chem.* **14**, 2542–2548 (2004).
- [62] Blesic, M., Saponjic, Z., Nedeljkovic, J., and Uskokovic, D. *Materials Letters* **54**(4), 298–302 (2002).
- [63] Wu, X., Jiang, Q.-Z., Ma, Z.-F., Fu, M., and Shang-guan, W.-F. *Solid State Communications* **136**(9-10), 513–517 (2005).
- [64] Archana, P. S., Gupta, A., Yusoff, M. M., and Jose, R. *Phys. Chem. Chem. Phys.* **16**, 7448–7454 (2014).
- [65] Xiaoyan, D., Chengwu, S., Yanru, Z., and Ni, W. *Journal of Semiconductors* **36**(7), 074003 (2015).
- [66] Kavan, L., Tétreault, N., Moehl, T., and Grätzel, M. *The Journal of Physical Chemistry C* **118**(30), 16408–16418 (2014).
- [67] Wu, Y., Yang, X., Chen, H., Zhang, K., Qin, C., Liu, J., Peng, W., Islam, A., Bi, E., Ye, F., Yin, M., Zhang, P., and Han, L. *Applied Physics Express* **7**(5), 052301 (2014).
- [68] Ke, W., Fang, G., Wang, J., Qin, P., Tao, H., Lei, H., Liu, Q., Dai, X., and Zhao, X. *ACS Applied Materials & Interfaces* **6**(18), 15959–15965 (2014).
- [69] Kavan, L., O'Regan, B., Kay, A., and Grätzel, M. *Journal of Electroanalytical Chemistry* **346**(1), 291–307 (1993).
- [70] Noh, J. H., Lee, S., Kim, J. Y., Lee, J.-K., Han, H. S., Cho, C. M., Cho, I. S., Jung, H. S., and Hong, K. S. *The Journal of Physical Chemistry C* **113**(3), 1083–1087 (2009).
- [71] Lee, S., Noh, J. H., Han, H. S., Yim, D. K., Kim, D. H., Lee, J.-K., Kim, J. Y., Jung, H. S., and Hong, K. S. *The Journal of Physical Chemistry C* **113**(16), 6878–6882 (2009).
- [72] Hoyer, R. L. Z., Musselman, K. P., and MacManus-Driscoll, J. L. *APL Materials* **1**(6), – (2013).
- [73] Duan, Y., Fu, N., Liu, Q., Fang, Y., Zhou, X., Zhang, J., and Lin, Y. *The Journal of Physical Chemistry C* **116**(16), 8888–8893 (2012).

- [74] De Angelis, F., Fantacci, S., Selloni, A., Nazeeruddin, M. K., and Gratzel, M. *The Journal of Physical Chemistry C* **114**(13), 6054–6061 (2010).
- [75] Meng, S. and Kaxiras, E. *Nano Letters* **10**(4), 1238–1247 (2010).
- [76] Brinker, C. J. and Scherer, G. W. *Sol-gel science, the physics and chemistry of sol-gel processing*. Academic Press, Boston, (1990).
- [77] Lamberti, A., Sacco, A., Bianco, S., Manfredi, D., Cappelluti, F., Hernandez, S., Quaglio, M., and Pirri, C. F. *Phys. Chem. Chem. Phys.* **15**, 2596–2602 (2013).
- [78] Duan, Y., Fu, N., Zhang, Q., Fang, Y., Zhou, X., and Lin, Y. *Electrochimica Acta* **107**(0), 473 – 480 (2013).
- [79] Ahmad, A., Buzby, S., Ni, C., and Shah, S. I. *Journal of Nanoscience and Nanotechnology* **8**(5), 2410–2418 (2008).
- [80] Alarcón, H., Hedlund, M., Johansson, E. M. J., Rensmo, H., Hagfeldt, A., and Boschloo, G. *The Journal of Physical Chemistry C* **111**(35), 13267–13274 (2007).
- [81] Ko, K. H., Lee, Y. C., and Jung, Y. J. *Journal of Colloid and Interface Science* **283**(2), 482–487 (2005).
- [82] Zhang, J., Han, Z., Li, Q., Yang, X., Yu, Y., and Cao, W. *Journal of Physics and Chemistry of Solids* **72**(11), 1239 – 1244 (2011).
- [83] Berglund, S. P., Hoang, S., Minter, R. L., Fullon, R. R., and Mullins, C. B. *The Journal of Physical Chemistry C* **117**(48), 25248–25258 (2013).
- [84] Earnshaw, A. and Greenwood, N. *Chemistry of the Elements (Second Edition)*. Elsevier Ltd., (1997).
- [85] Nada, M., Gonda, T., Shen, Q., Shimada, H., Toyoda, T., and Kobayashi, N. *Japanese Journal of Applied Physics* **48**(2R), 025505 (2009).
- [86] Subramanian, A., Bow, J. S., and Wang, H. W. *Thin Solid Films* **520**(23), 7011–7017 (2012).
- [87] Iwamoto, S., Sazanami, Y., Inoue, M., Inoue, T., Hoshi, T., Shigaki, K., Kaneko, M., and Maenosono, A. *ChemSusChem* **1**(5), 401–403 (2008).
- [88] Kakiage, K., Tokutome, T., Iwamoto, S., Kyomen, T., and Hanaya, M. *Chemical Communications* **49**(2), 179–180 (2013).
- [89] Zhang, C., Chen, S., Mo, L., Huang, Y., Tian, H., Hu, L., Huo, Z., Dai, S., Kong, F., and Pan, X. *The Journal of Physical Chemistry C* **115**(33), 16418–16424 (2011).
- [90] Liu, Q. P., Zhou, Y., Duan, Y. D., Wang, M., and Lin, Y. *Electrochimica Acta* **95**, 48–53 (2013).
- [91] Liu, Q., Zhou, Y., Duan, Y., Wang, M., Zhao, X., and Lin, Y. *Journal of Alloys and Compounds* **548**(0), 161 – 165 (2013).
- [92] Pan, M., Liu, H., Yao, Z., and Zhong, X. *Journal of Nanomaterials* **2015**, 974161 (2015).
- [93] Li, W., Yang, J., Zhang, J., Gao, S., Luo, Y., and Liu, M. *Materials Research Bulletin* **57**(0), 177 – 183 (2014).
- [94] Watson, D. F. and Meyer, G. J. *Coordination Chemistry Reviews* **248**(1314), 1391 – 1406 (2004).
- [95] Kalyanasundaram, K. *Dye-Sensitized Solar Cells*. EPFL Press, first edition, (2010).
- [96] Jin, Z.-L. and Lu, G.-X. *Journal of Inorganic Materials* **26**(6), 571 (2011).
- [97] Tian, H., Hu, L., Zhang, C., Chen, S., Sheng, J., Mo, L., Liu, W., and Dai, S. *J. Mater. Chem.* **21**, 863–868 (2011).
- [98] Tian, H., Hu, L., Li, W., Sheng, J., Xu, S., and Dai, S. *J. Mater. Chem.* **21**, 7074–7077 (2011).
- [99] Im, J. S., Yun, J., Lee, S. K., and Lee, Y.-S. *Journal of Alloys and Compounds* **513**(0), 573 – 579 (2012).
- [100] Subramanian, A. and Wang, H.-W. *Applied Surface Science* **258**(17), 6479 – 6484 (2012).
- [101] Nguyen, T.-V., Lee, H.-C., Khan, M. A., and Yang, O.-B. *Solar Energy* **81**(4), 529 – 534 (2007).
- [102] Imahori, H., Hayashi, S., Umeyama, T., Eu, S., Oguro, A., Kang, S., Matano, Y., Shishido, T., Ngamsinlapasathian, S., and Yoshikawa, S. *Langmuir* **22**(26), 11405–11411 (2006).
- [103] Wang, M., Bai, S., Chen, A., Duan, Y., Liu, Q., Li, D., and Lin, Y. *Electrochimica Acta* **77**(0), 54–59 (2012).
- [104] Chen, D., Yang, D., Wang, Q., and Jiang, Z. *Industrial & Engineering Chemistry Research* **45**(12), 4110–4116 (2006).
- [105] Finazzi, E., Di Valentin, C., and Pacchioni, G. *The Journal of Physical Chemistry C* **113**(1), 220–228 (2009).
- [106] Chu, D., Yuan, X., Qin, G., Xu, M., Zheng, P., Lu, J., and Zha, L. *Journal of Nanoparticle Research* **10**(2), 357–363 (2008).
- [107] Hsu, C.-W., Chen, P., and Ting, J.-M. *Journal of the Electrochemical Society* **160**(3), H160–H165 (2013).
- [108] Lindgren, T., Mwabora, J. M., Avendao, E., Jonsson, J., Hoel, A., Granqvist, C.-G., and Lindquist, S.-E. *The Journal of Physical Chemistry B* **107**(24), 5709–5716 (2003).
- [109] Wang, X., Yang, Y., Jiang, Z., and Fan, R. *European Journal of Inorganic Chemistry* **2009**(23), 3481–3487 (2009).
- [110] Zhang, J., Sun, Q., Zheng, J., Zhang, X., Cui, Y., Wang, P., Li, W., and Zhu, Y. *Journal of Renewable and Sustainable Energy* **3**(3), 033108 (2011).
- [111] Zhang, J., Zheng, X., Yang, X., and Cao, W. *Journal of Inorganic and Organometallic Polymers and Materials* **21**(1), 150–156 (2011).
- [112] Umar, A. A., Rahman, M. Y. A., Saad, S. K. M., and Salleh, M. M. *International Journal of Electrochemical Science* **7**(9), 7855–7865 (2012).
- [113] Liu, W., Feng, Z., and Cao, W. *Research on Chemical Intermediates* **39**(4), 1623–1631 (2013).
- [114] Diker, H., Varlikli, C., and Stathatos, E. *International Journal of Energy Research* **38**(7), 908–917 (2014).
- [115] D. A. Duarte, M. M. and da Silva Sobrinho, A. S. *International Journal of Photoenergy* (2014).
- [116] Lim, S. P., Pandikumar, A., Huang, N. M., Lim, H. N., Gu, G., and Ma, T. L. *RSC Adv.* **4**, 48236–48244 (2014).

- [117] Mekprasart, W., Suphankij, S., Tangcharoen, T., Simpraditpan, A., and Pecharapa, W. *physica status solidi (a)* **211**(8), 1745–1751 (2014).
- [118] Simya, O., Selvam, M., Karthik, A., and Rajendran, V. *Synthetic Metals* **188**(0), 124 – 129 (2014).
- [119] Kushwaha, R., Chauhan, R., Srivastava, P., and Bahadur, L. *Journal of Solid State Electrochemistry* **19**(2), 507–517 (2015).
- [120] Zheng, X., Zhang, J., Peng, L., Yang, X., and Cao, W. *Journal of Materials Science* **46**(15), 5071–5078 (2011).
- [121] Ma, T., Akiyama, M., Abe, E., and Imai, I. *Nano Letters* **5**(12), 2543–2547 (2005). PMID: 16351212.
- [122] Melhem, H., Simon, P., Wang, J., Bin, C. D., Ratier, B., Leconte, Y., Herlin-Boime, N., Makowska-Janusik, M., Kassiba, A., and Bouclé, J. *Solar Energy Materials and Solar Cells* **117**(0), 624 – 631 (2013).
- [123] Kang, S. H., Kim, H. S., Kim, J.-Y., and Sung, Y.-E. *Materials Chemistry and Physics* **124**(1), 422 – 426 (2010).
- [124] Eom, K. H., Yun, T. K., Hong, J.-Y., Bae, J. Y., Huh, S., and Won, Y. S. *Journal of Nanoscience and Nanotechnology* **14**(12), 9362–9367 (2014).
- [125] Guo, W., Shen, Y., Boschloo, G., Hagfeldt, A., and Ma, T. *Electrochimica Acta* **56**(12), 4611 – 4617 (2011).
- [126] Fu, Z., Zhang, J., Yang, X., and Cao, W. *Chinese Science Bulletin* **56**(19), 2001–2008 (2011).
- [127] Qi, L., Li, C., and Chen, Y. *Chemical Physics Letters* **539540**(0), 128 – 132 (2012).
- [128] Li, Y., Jia, L., Wu, C., Han, S., Gong, Y., Chi, B., Pu, J., and Jian, L. *Journal of Alloys and Compounds* **512**(1), 23 – 26 (2012).
- [129] Lim, C. K., Huang, H., Chow, C. L., Tan, P. Y., Chen, X., Tse, M. S., and Tan, O. K. *The Journal of Physical Chemistry C* **116**(37), 19659–19664 (2012).
- [130] Zhang, J., Fu, Z., Lv, Q., Yang, X., and Cao, W. *Journal of Sol-Gel Science and Technology* **63**(3), 554–562 (2012).
- [131] Qin, W., Lu, S., Wu, X., and Wang, S. *International Journal of Electrochemical Science* **8**(6), 7984–7990 (2013).
- [132] Wang, H., Li, H., Wang, J., Wu, J., Li, D., Liu, M., and Su, P. *Electrochimica Acta* **137**(0), 744 – 750 (2014).
- [133] Guo, W., Wu, L., Chen, Z., Boschloo, G., Hagfeldt, A., and Ma, T. *Journal of Photochemistry and Photobiology A: Chemistry* **219**(23), 180 – 187 (2011).
- [134] Guo, W., Shen, Y., Wu, L., Gao, Y., and Ma, T. *The Journal of Physical Chemistry C* **115**(43), 21494–21499 (2011).
- [135] Yun, Tae Kwan; Cheon, J. H. B. J. Y. A. K.-S. K. J. H. *Journal of Nanoscience and Nanotechnology* **12**(4), 3305–3308 (2012).
- [136] Park, S. K., Yun, T. K., Bae, J. Y., and Won, Y. S. *Applied Surface Science* **285**, Part B(0), 789 – 794 (2013).
- [137] Xie, Y., Huang, N., Liu, Y., Sun, W., Mehnane, H. F., You, S., Wang, L., Liu, W., Guo, S., and Zhao, X.-Z. *Electrochimica Acta* **93**(0), 202 – 206 (2013).
- [138] Huo, J., Hu, Y., Jiang, H., Hou, X., and Li, C. *Chemical Engineering Journal* **258**(0), 163 – 170 (2014).
- [139] Motlak, M., Akhtar, M. S., Barakat, N. A., Hamza, A., Yang, O.-B., and Kim, H. Y. *Electrochimica Acta* **115**(0), 493 – 498 (2014).
- [140] Park, J. Y., Lee, K. H., Kim, B. S., Kim, C. S., Lee, S. E., Okuyama, K., Jang, H. D., and Kim, T. O. *Rsc Advances* **4**(20), 9946–9952 (2014).
- [141] Yu, J., Yang, Y., Fan, R., Li, L., and Li, X. *The Journal of Physical Chemistry C* **118**(17), 8795–8802 (2014).
- [142] Guo, E. and Yin, L. *Phys. Chem. Chem. Phys.* **17**, 563–574 (2015).
- [143] Tian, H., Hu, L., Zhang, C., Liu, W., Huang, Y., Mo, L., Guo, L., Sheng, J., and Dai, S. *The Journal of Physical Chemistry C* **114**(3), 1627–1632 (2010).
- [144] Noh, S. I., Bae, K.-N., Ahn, H.-J., and Seong, T.-Y. *Ceramics International* **39**(7), 8097 – 8101 (2013).
- [145] Neo, C. Y. and Ouyang, J. *Journal of Power Sources* **241**(0), 647 – 653 (2013).
- [146] Song, J., Yang, H. B., Wang, X., Khoo, S. Y., Wong, C. C., Liu, X.-W., and Li, C. M. *ACS Applied Materials & Interfaces* **4**(7), 3712–3717 (2012).
- [147] Duan, Y., Zheng, J., Xu, M., Song, X., Fu, N., Fang, Y., Zhou, X., Lin, Y., and Pan, F. *J. Mater. Chem. A* **3**, 5692–5700 (2015).
- [148] Hou, Q., Zheng, Y., Chen, J.-F., Zhou, W., Deng, J., and Tao, X. *Journal of Materials Chemistry* **21**(11), 3877–3883 (2011).
- [149] Tojo, S., Tachikawa, T., Fujitsuka, M., and Majima, T. *The Journal of Physical Chemistry C* **112**(38), 14948–14954 (2008).
- [150] Liu, G., Sun, C., Yan, X., Cheng, L., Chen, Z., Wang, X., Wang, L., Smith, S. C., Lu, G. Q. M., and Cheng, H.-M. *J. Mater. Chem.* **19**, 2822–2829 (2009).
- [151] Niu, M., Cui, R., Wu, H., Cheng, D., and Cao, D. *The Journal of Physical Chemistry C* **119**(24), 13425–13432 (2015).
- [152] Latini, A., Cavallo, C., Aldibaja, F. K., Gozzi, D., Carta, D., Corrias, A., Lazzarini, L., and Salviati, G. *Journal of Physical Chemistry C* **117**(48), 25276–25289 (2013).
- [153] Liu, Z., Li, Y., Liu, C., Ya, J., E, L., Zhao, W., Zhao, D., and An, L. *ACS Applied Materials & Interfaces* **3**(5), 1721–1725 (2011).
- [154] Liu, J., Duan, Y., Zhou, X., and Lin, Y. *Applied Surface Science* **277**(0), 231 – 236 (2013).
- [155] Seo, H., Wang, Y., Ichida, D., Uchida, G., Itagaki, N., Koga, K., Shiratani, M., Nam, S.-H., and Boo, J.-H. *Japanese Journal of Applied Physics* **52**(11S), 11NM02 (2013).
- [156] Xie, Y., Huang, N., You, S., Liu, Y., Sebo, B., Liang, L., Fang, X., Liu, W., Guo, S., and Zhao, X.-Z. *Journal of Power Sources* **224**(0), 168–173 (2013).
- [157] Mohammadi, M. R., Bakhshayesh, A. M., Sadri, F., and Masroor, M. *Journal of Sol-Gel Science and Technology* **67**(1), 77–87 (2013).
- [158] Kim, C., Kim, K. S., Kim, H. Y., and Han, Y. S. *Journal of Materials Chemistry* **18**(47), 5809–5814 (2008).

- [159] Liao, L. C.-K. and Lin, C.-C. *Thin Solid Films* **516**(8), 1998 – 2002 (2008).
- [160] Shalan, A. and Rashad, M. *Applied Surface Science* **283**(0), 975 – 981 (2013).
- [161] Shin, S. G., Bark, C. W., and Choi, H. W. *Molecular Crystals and Liquid Crystals* **600**(1), 47–55 (2014).
- [162] Yacoubi, B., Samet, L., Bennaceur, J., Lamouchi, A., and Chtourou, R. *Materials Science in Semiconductor Processing* **30**(0), 361 – 367 (2015).
- [163] Eom, T. S., Kim, K. H., Bark, C. W., and Choi, H. W. *Molecular Crystals and Liquid Crystals* **600**(1), 39–46 (2014).
- [164] Liao, L. C.-K. and Lin, C.-C. *Applied Surface Science* **253**(21), 8798 – 8801 (2007).
- [165] Archana, P. S., Naveen Kumar, E., Vijila, C., Ramakrishna, S., Yusoff, M. M., and Jose, R. *Dalton Trans.* **42**, 1024–1032 (2013).
- [166] Malik, A., Hameed, S., Siddiqui, M. J., Haque, M. M., Umar, K., Khan, A., and Muneer, M. *Journal of Materials Engineering and Performance* **23**(9), 3184–3192 (2014).
- [167] Zainudin, S. N. F., Markom, M., and Abdullah, H. *Advanced Materials Conference (AMS 2012)* **879**, 199–205 (2014).
- [168] Wijayarathna, T. R. C. K., Aponso, G. M. L. P., Ariyasinghe, Y. P. Y. P., Premalal, E. V. A., Kumara, G. K. R., and Tennakone, K. *Nanotechnology* **19**(48), 485703 (2008).
- [169] Navas, J., Fernandez-Lorenzo, C., Aguilar, T., Alcantara, R., and Martin-Calleja, J. *Physica Status Solidi a-Applications and Materials Science* **209**(2), 378–385 (2012).
- [170] Wang, Y., Hao, Y., Cheng, H., Ma, J., Xu, B., Li, W., and Cai, S. *Journal of Materials Science* **34**(12), 2773–2779 (1999).
- [171] Zhang, J. C., Fu, C. Y., Yang, X. Y., and Cao, W. L. *Journal of Inorganic and Organometallic Polymers and Materials* **21**(1), 43–49 (2011).
- [172] Wang, K.-P. and Teng, H. *Physical Chemistry Chemical Physics* **11**(41), 9489–9496 (2009).
- [173] Zhang, Y., Wang, L., Liu, B., Zhai, J., Fan, H., Wang, D., Lin, Y., and Xie, T. *Electrochimica Acta* **56**(18), 6517–6523 (2011).
- [174] Zhang, X., Wang, S.-T., and Wang, Z.-S. *Applied Physics Letters* **99**(11), 113503 (2011).
- [175] Zhu, F., Zhang, P., Wu, X., Fu, L., Zhang, J., and Xu, D. *ChemPhysChem* **13**(16), 3731–3737 (2012).
- [176] Zhu, G., Cheng, Z., Lv, T., Pan, L., Zhao, Q., and Sun, Z. *Nanoscale* **2**(7), 1229–1232 (2010).
- [177] Niaki, A. H. G., Bakhshayesh, A. M., and Mohammedi, M. R. *Solar Energy* **103**, 210–222 (2014).
- [178] Ali, Z., Park, K. H., Shakir, I., and Kang, D. J. *Electrochimica Acta* **161**(0), 329 – 334 (2015).
- [179] Chen, S., Lin, J., and Wu, J. *Applied Surface Science* **293**(0), 202 – 206 (2014).
- [180] Chen, S., Lin, J., and Wu, J. *Journal of Materials Science: Materials in Electronics* **25**(5), 2060–2065 (2014).
- [181] Chandiran, A. K., Sauvage, F., Etgar, L., and Grätzel, M. *The Journal of Physical Chemistry C* **115**(18), 9232–9240 (2011).
- [182] Kitiyanan, A., Ngamsinlapasathian, S., Pavasupree, S., and Yoshikawa, S. *Journal of Solid State Chemistry* **178**(4), 1044–1048 (2005).
- [183] Diirr, M., Rosselli, S., Yasuda, A., and Nelles, G. *The Journal of Physical Chemistry B* **110**(43), 21899–21902 (2006).
- [184] Archana, P. S., Gupta, A., Yusoff, M. M., and Jose, R. *Applied Physics Letters* **105**(15) (2014).
- [185] Archana, P. S., Jose, R., Jin, T. M., Vijila, C., Yusoff, M. M., and Ramakrishna, S. *Journal of the American Ceramic Society* **93**(12), 4096–4102 (2010).
- [186] Lü, X., Mou, X., Wu, J., Zhang, D., Zhang, L., Huang, F., Xu, F., and Huang, S. *Advanced Functional Materials* **20**(3), 509–515 (2010).
- [187] Tsvetkov, N., Larina, L., Shevaleevskiy, O., and Ahn, B. T. *Energy & Environmental Science* **4**(4), 1480–1486 (2011).
- [188] Tsvetkov, N., Larina, L., Shevaleevskiy, O., and Ahn, B. *Journal of the Electrochemical Society* **158**(11), B1281–B1285 (2011).
- [189] Kim, S. G., Ju, M. J., Choi, I. T., Choi, W. S., Choi, H. J., Baek, J. B., and Kim, H. K. *Rsc Advances* **3**(37), 16380–16386 (2013).
- [190] Chandiran, A. K., Sauvage, F., Casas-Cabanas, M., Comte, P., Zakeeruddin, S. M., and Grätzel, M. *The Journal of Physical Chemistry C* **114**(37), 15849–15856 (2010).
- [191] Long, L., Wu, L., Yang, X., and Li, X. *Journal of Materials Science & Technology* **30**(8), 765 – 769 (2014).
- [192] Luo, J., Zhou, J., Guo, H., Yang, W., Liao, B., Shi, W., and Chen, Y. *RSC Adv.* **4**, 56318–56322 (2014).
- [193] Liu, J., Yang, H., Tan, W., Zhou, X., and Lin, Y. *Electrochimica Acta* **56**(1), 396–400 (2010).
- [194] Choi, J. H., Kwon, S. H., Jeong, Y. K., Kim, I., and Kim, K. H. *Journal of the Electrochemical Society* **158**(6), 749–753 (2011).
- [195] Ghosh, R., Hara, Y., Alibabaei, L., Hanson, K., Rangan, S., Bartynski, R., Meyer, T. J., and Lopez, R. *ACS Applied Materials & Interfaces* **4**(9), 4566–4570 (2012).
- [196] Kao, M.-C., Chen, H.-Z., and Young, S.-L. *Japanese Journal of Applied Physics* **52**(1S), 01AD04 (2013).
- [197] Lee, K. and Schmuki, P. *Electrochemistry Communications* **25**(0), 11–14 (2012).
- [198] Zhang, X., Liu, F., Huang, Q.-L., Zhou, G., and Wang, Z.-S. *The Journal of Physical Chemistry C* **115**(25), 12665–12671 (2011).
- [199] Kamisaka, H., Suenaga, T., Nakamura, H., and Yamashita, K. *The Journal of Physical Chemistry C* **114**(29), 12777–12783 (2010).
- [200] Cant, A. M., Huang, F. Z., Zhang, X. L., Chen, Y., Cheng, Y. B., and Amal, R. *Nanoscale* **6**(7), 3875–3880 (2014).
- [201] Yang, J. H., Kim, K. H., Bark, C. W., and Choi, H. W. *Molecular Crystals and Liquid Crystals* **598**(1), 32–39 (2014).

- [202] Tong, Z., Peng, T., Sun, W., Liu, W., Guo, S., and Zhao, X.-Z. *The Journal of Physical Chemistry C* **118**(30), 16892–16895 (2014).
- [203] Grätzel, M. *Nature* **414**(6861), 338–344 (2001).
- [204] Furubayashi, Y., Hitosugi, T., Yamamoto, Y., Inaba, K., Kinoda, G., Hirose, Y., Shimada, T., and Hasegawa, T. *Applied Physics Letters* **86**(25), 252101 (2005).
- [205] Hirano, M. and Matsushima, K. *Journal of Nanoscience and Nanotechnology* **6**(3), 762–770 (2006).
- [206] Hou, X.-G., Liu, A.-D., Huang, M.-D., Liao, B., and Wu, X.-L. *Chinese Physics Letters* **26**(7), 077106 (2009).
- [207] Kavan, L., Grätzel, M., Gilbert, S. E., Klemenz, C., and Scheel, H. J. *Journal of the American Chemical Society* **118**(28), 6716–6723 (1996).
- [208] Huang, F., Cheng, Y.-B., and Caruso, R. *Australian Journal of Chemistry* **64**(6), 820–824 (2011).
- [209] Manoharan, K. and Venkatachalam, P. *Materials Science in Semiconductor Processing* **30**(0), 208 – 217 (2015).
- [210] Bakhshayesh, A. and Farajisafilo, N. *Applied Surface Science* **331**(0), 58 – 65 (2015).
- [211] Sun, X. H., Zhang, Q. L., Liu, Y. M., Huang, N., Sun, P. P., Peng, T., Peng, T. Y., and Zhao, X. Z. *Electrochimica Acta* **129**, 276–282 (2014).
- [212] Yun, S., Lee, J., Chung, J., and Lim, S. *Journal of Physics and Chemistry of Solids* **71**(12), 1724 – 1731 (2010).
- [213] Augustynski, J., Hinden, J., and Stalder, C. *Journal of The Electrochemical Society* **124**(7), 1063–1064 (1977).
- [214] Strange, P., Svane, A., Temmerman, W. M., Szotek, Z., and Winter, H. *Nature* **399**(6738), 756–758 (1999).
- [215] Auzel, F. *Chemical Reviews* **104**(1), 139–174 (2004).
- [216] Strümpel, C., McCann, M., Beaucarne, G., Arkhipov, V., Slaoui, A., Svrcek, V., del Canizo, C., and Tobias, I. *Solar Energy Materials and Solar Cells* **91**(4), 238 – 249 (2007).
- [217] Wang, J., Ming, T., Jin, Z., Wang, J., Sun, L.-D., and Yan, C.-H. *Nat Commun* **5** (2014).
- [218] Masuda, Y., Yamagishi, M., and Koumoto, K. *Chemistry of Materials* **19**(5), 1002–1008 (2007).
- [219] Wu, X.-H., Wang, S., Guo, Y., Xie, Z.-Y., Han, L., and Jiang, Z.-H. *Chinese Journal of Chemistry* **26**(10), 1939–1943 (2008).
- [220] Zhang, J., Zhao, Z., Wang, X., Yu, T., Guan, J., Yu, Z., Li, Z., and Zou, Z. *The Journal of Physical Chemistry C* **114**(43), 18396–18400 (2010).
- [221] Yahav, S., Rühle, S., Greenwald, S., Barad, H.-N., Shalom, M., and Zaban, A. *The Journal of Physical Chemistry C* **115**(43), 21481–21486 (2011).
- [222] Zhang, J., Peng, W., Chen, Z., Chen, H., and Han, L. *The Journal of Physical Chemistry C* **116**(36), 19182–19190 (2012).
- [223] Zhang, J., Feng, J., Hong, Y., Zhu, Y., and Han, L. *Journal of Power Sources* **257**(0), 264 – 271 (2014).
- [224] Yao, Q., Liu, J., Peng, Q., Wang, X., and Li, Y. *Chemistry An Asian Journal* **1**(5), 737–741 (2006).
- [225] Hafez, H., Saif, M., and Abdel-Mottaleb, M. *Journal of Power Sources* **196**(13), 5792 – 5796 (2011).
- [226] Li, Q. B., Lin, J. M., Wu, J. H., Lan, Z., Wang, Y., Peng, F. G., and Huang, M. L. *Journal of Luminescence* **134**, 59–62 (2013).
- [227] Hafez, H., Wu, J., Lan, Z., Li, Q., Xie, G., Lin, J., Huang, M., and Yunfang Huang and, M. S. A.-M. *Nanotechnology* **21**(41), 415201 (2010).
- [228] Wu, J., Xie, G., Lin, J., Lan, Z., Huang, M., and Huang, Y. *Journal of Power Sources* **195**(19), 6937 – 6940 (2010).
- [229] Huang, S. H. *Journal of the American Ceramic Society* **96**(10), 3108–3113 (2013).
- [230] Wu, J. H., Wang, J. L., Lin, J. M., Xiao, Y. M., Yue, G. T., Huang, M. L., Lan, Z., Huang, Y. F., Fan, L. Q., Yin, S., and Sato, T. *Scientific Reports* **3**, 5 (2013).
- [231] Shan, G.-B. and Demopoulos, G. P. *Advanced Materials* **22**(39), 4373–4377 (2010).
- [232] Xie, G. X., Lin, J. M., Wu, J. H., Lan, Z., Li, Q. H., Xiao, Y. M., Yue, G. T., Yue, H. F., and Huang, M. L. *Chinese Science Bulletin* **56**(1), 96–101 (2011).
- [233] Wang, J. L., Wu, J. H., Lin, J. M., Huang, M. L., Huang, Y. F., Lan, Z., Xiao, Y. M., Yue, G. T., Yin, S., and Sato, T. *Chemsuschem* **5**(7), 1307–1312 (2012).
- [234] Wu, J., Wang, J., Lin, J., Lan, Z., Tang, Q., Huang, M., Huang, Y., Fan, L., Li, Q., and Tang, Z. *Advanced Energy Materials* **2**(1), 78–81 (2012).
- [235] Wang, J. L., Lin, J. M., Wu, J. H., Huang, M. L., Lan, Z., Chen, Y., Tang, S., Fan, L. Q., and Huang, Y. F. *Electrochimica Acta* **70**, 131–135 (2012).
- [236] Yu, J., Yang, Y., Fan, R., Zhang, H., Li, L., Wei, L., Shi, Y., Pan, K., and Fu, H. *Journal of Power Sources* **243**(0), 436–443 (2013).
- [237] Li, Q. B., Lin, J. M., Wu, J. H., Lan, Z., Wang, Y., Peng, F. G., and Huang, M. L. *Electrochimica Acta* **56**(14), 4980–4984 (2011).
- [238] Xie, G. X., Wei, Y. L., Fan, L. Q., Wu, J. H., and Iop. *4th International Symposium on Functional Materials (Isfm2011)* **339**, 4 (2012).
- [239] Xu, W.-W., Dai, S.-Y., Hu, L.-H., Liang, L.-Y., and Wang, K.-J. *Chinese Physics Letters* **23**(8), 2288 (2006).
- [240] Liqiang, J., Xiaojun, S., Baifu, X., Baiqi, W., Weimin, C., and Honggang, F. *Journal of Solid State Chemistry* **177**(10), 3375 – 3382 (2004).
- [241] Chen, S. W., Lee, J. M., Lu, K. T., Pao, C. W., Lee, J. F., Chan, T. S., and Chen, J. M. *Applied Physics Letters* **97**(1), 012104 (2010).
- [242] Eperon, G. E., Burlakov, V. M., Docampo, P., Goriely, A., and Snaith, H. J. *Advanced Functional Materials* **24**(1), 151–157 (2014).
- [243] Wang, J., Qin, M., Tao, H., Ke, W., Chen, Z., Wan, J., Qin, P., Xiong, L., Lei, H., Yu, H., and Fang, G. *Applied Physics Letters* **106**(12) (2015).

- [244] Kim, D. H., Han, G. S., Seong, W. M., Lee, J.-W., Kim, B. J., Park, N.-G., Hong, K. S., Lee, S., and Jung, H. S. *ChemSusChem* (2015).
- [245] Oku, T., Iwata, T., and Suzuki, A. *Chemistry Letters* **44**(7), 1033–1035 (2015).
- [246] Qin, P., Domanski, A. L., Chandiran, A. K., Berger, R., Butt, H.-J., Dar, M. I., Moehl, T., Tetreault, N., Gao, P., Ahmad, S., Nazeeruddin, M. K., and Grätzel, M. *Nanoscale* **6**, 1508–1514 (2014).
- [247] Zhou, H., Chen, Q., Li, G., Luo, S., Song, T.-b., Duan, H.-S., Hong, Z., You, J., Liu, Y., and Yang, Y. *Science* **345**(6196), 542–546 (2014).
- [248] Nagaoka, H., Ma, F., deQuilettes, D. W., Vorpahl, S. M., Glaz, M. S., Colbert, A. E., Ziffer, M. E., and Ginger, D. S. *The Journal of Physical Chemistry Letters* **6**(4), 669–675 (2015).
- [249] Wehrenfennig, C., Liu, M., Snaith, H. J., Johnston, M. B., and Herz, L. M. *Energy Environ. Sci.* **7**, 2269–2275 (2014).
- [250] Chen, H.-W., Sakai, N., Ikegami, M., and Miyasaka, T. *The Journal of Physical Chemistry Letters* **6**(1), 164–169 (2015).
- [251] Unger, E. L., Hoke, E. T., Bailie, C. D., Nguyen, W. H., Bowring, A. R., Heumüller, T., Christoforo, M. G., and McGehee, M. D. *Energy Environ. Sci.* **7**, 3690–3698 (2014).
- [252] Kim, H.-S., Mora-Sero, I., Gonzalez-Pedro, V., Fabregat-Santiago, F., Juarez-Perez, E. J., Park, N.-G., and Bisquert, J. *Nat Commun* **4** (2013).
- [253] Dualeh, A., Moehl, T., Tetreault, N., Teuscher, J., Gao, P., Nazeeruddin, M. K., and Grätzel, M. *ACS Nano* **8**(1), 362–373 (2014).
- [254] Kim, H.-S. and Park, N.-G. *The Journal of Physical Chemistry Letters* **5**(17), 2927–2934 (2014).
- [255] Tress, W., Marinova, N., Moehl, T., Zakeeruddin, S. M., Nazeeruddin, M. K., and Grätzel, M. *Energy Environ. Sci.* **8**, 995–1004 (2015).
- [256] Shao, Y., Xiao, Z., Bi, C., Yuan, Y., and Huang, J. *Nat Commun* **5** (2014).
- [257] Assadi, M. H. N. and Hanaor, D. A. H. *Journal of Applied Physics* **113**(23) (2013).
- [258] Rietveld, H. M. *Journal of Applied Crystallography* **2**(2), 65–71 (1969).
- [259] Scherrer, P. *Göttinger Nachrichten Gesell.* **2**, 98 (1918).
- [260] Patterson, A. *Phys. Rev.* **56**, 978–982 Nov (1939).
- [261] Bragg, W. L. *Proceedings of the Cambridge Philosophical Society* **17**, 43–57 (1913).
- [262] Gaudon, M., Toulemonde, O., and Demourgues, A. *Inorganic Chemistry* **46**(26), 10996–11002 (2007).
- [263] Denton, A. and Ashcroft, N. *Phys. Rev. A* **43**, 3161–3164 Mar (1991).
- [264] Brunauer, S., Emmett, P. H., and Teller, E. *Journal of the American Chemical Society* **60**(2), 309–319 (1938).
- [265] Barrett, E. P., Joyner, L. G., and Halenda, P. P. *Journal of the American Chemical Society* **73**(1), 373–380 (1951).
- [266] Escobedo Morales, A.; Sánchez Mora, E. P. U. *Revista Mexicana de Física Supplement* **53**(5), 18–22 (2007).
- [267] Kubelka, P. and Munk, F. *Zeitschrift für technische Physik* **12**, 593–601 (1931).
- [268] Tauc, J. *Materials Research Bulletin* **3**(1), 37 – 46 (1968).
- [269] Choudhury, B. and Choudhury, A. *Materials Chemistry and Physics* **132**(23), 1112 – 1118 (2012).
- [270] Alarcón, H., Boschloo, G., Mendoza, P., Solis, J. L., and Hagfeldt, A. *The Journal of Physical Chemistry B* **109**(39), 18483–18490 (2005).
- [271] Hall, E. H. *American Journal of Mathematics* **2**(3), 287–292 (1879).
- [272] Popovic, R. S. *Hall Effect Devices: Magnetic Sensors and Characterization of Semiconductors (Series in Sensors)*. Taylor & Francis, (1991).
- [273] Hurum, D., Agrios, A., Crist, S., Gray, K., Rajh, T., and Thurnauer, M. *Journal of Electron Spectroscopy and Related Phenomena* **150**(2-3), 155 – 163 (2006).
- [274] Barnes, P. R. F., Miettunen, K., Li, X., Anderson, A. Y., Bessho, T., Grätzel, M., and O'Regan, B. C. *Advanced Materials* **25**(13), 1881–1922 (2013).
- [275] Sarker, S., Ahammad, A. J. S., Seo, H. W., and Kim, D. M. *International Journal of Photoenergy* (2014).
- [276] Cao, F., Oskam, G., Meyer, G. J., and Searson, P. C. *The Journal of Physical Chemistry* **100**(42), 17021–17027 (1996).
- [277] van de Lagemaat, J. and Frank, A. J. *The Journal of Physical Chemistry B* **105**(45), 11194–11205 (2001).
- [278] Schlichthörl, G., Huang, S. Y., Sprague, J., and Frank, A. J. *The Journal of Physical Chemistry B* **101**(41), 8141–8155 (1997).
- [279] Zaban, A., Greenshtein, M., and Bisquert, J. *ChemPhysChem* **4**(8), 859–864 (2003).
- [280] Boschloo, G., Häggman, L., and Hagfeldt, A. *The Journal of Physical Chemistry B* **110**(26), 13144–13150 (2006).
- [281] Boschloo, G. and Hagfeldt, A. *The Journal of Physical Chemistry B* **109**(24), 12093–12098 (2005).
- [282] O'Regan, B. C., Scully, S., Mayer, A. C., Palomares, E., and Durrant, J. *The Journal of Physical Chemistry B* **109**(10), 4616–4623 (2005).
- [283] Gelderman, K., Lee, L., and Donne, S. W. *Journal of Chemical Education* **84**(4), 685 (2007).
- [284] van de Lagemaat, J., Park, N.-G., and Frank, A. J. *The Journal of Physical Chemistry B* **104**(9), 2044–2052 (2000).